Modeling Permafrost Thaw Dynamics: A Conceptual and Energy-Based Approach

A THESIS

SUBMITTED TO THE FACULTY OF THE GRADUATE SCHOOL

OF THE UNIVERSITY OF MINNESOTA

BY

María Isabel Sánchez Muñiz

IN PARTIAL FULFILLMENT OF THE REQUIREMENTS

FOR THE DEGREE OF

DOCTOR OF PHILOSOPHY

Richard McGehee

February, 2025

Acknowledgements

First and foremost, I wish to express my heartfelt gratitude to my advisor, Professor Dick McGehee, whose presence in my life has extended far beyond the academic realm. His unwavering support guided me through not just my research, but through the unprecedented challenges of the COVID-19 pandemic and life's most precious moments - from sharing in my wedding day to offering steadfast support during my pregnancy and the birth of my daughter. Through our work on climate change research, he has shown me what it means to approach complex problems with both intellectual rigor and meaningful purpose, providing me with direction that sustained me through graduate school. His exceptional blend of scientific excellence and genuine humanity has set an inspiring example of the kind of mentor and scientist I aspire to become. It has been a profound privilege to be his student, and I carry forward both immense gratitude and pride in having been part of his academic lineage. I also thank my committee members, Paul Garrett, Kaitlin Hill, and, Arnd Scheel, for reading my thesis and providing valuable feedback.

To my academic siblings, Grace Zhang, Yorkinoy Shermatova (and Sunnat and

Sarvar), Cameron Thieme, Ty Frazier, Gisell Ayala, Jasmine Noory, Daniela Beckelhymer, and Kate Meyer, thank you for your friendship and encouragement.

I want to thank my office mates, Shannon Negaard-Paper, McCleary Philbin, and Shengmai Ann, for their support. To colleagues Samuel Magill, Bryan Felix, Dorian Smith, and Adrienne Sands, as well as Minnesota friends Fernando Rodriguez, Tor Chavarria, and Jemma Larson, thank you for your friendship.

To my Puerto Rican family in Minnesota, Ivan Fontanez, Jeannette Miranda, Silvina, Regina, and Tamara Ramirez, thank you for making me feel at home. To my best friend, Dimary Cubero, thank you for your steadfast support over the years. To my cousin, Dr. Ruben Lastra, thank you for showing that a science Ph.D. in the cold Midwest. To my enduring support system from CCNY: Samuel Magill, Giancarlo Paolillo, Benjamin Steinberg, Pat Hooper, Brooke Feigon, and Thea Pignataro - thank you for over a decade of mentorship and friendship, from my undergraduate years through my current role as a lecturer. Your guidance and encouragement helped shape my mathematical journey and gave me the confidence to pursue this doctorate, while your continued support as colleagues has enriched my teaching experience.

I thank my parents, sisters, Titi Lourdes, Tio Papo, and Abuelas Gladys and Malen for their love and support. To my Abuela Gladys and Abuela Malen, thank you for your love and support.

Lastly, I want to thank my husband, Chen, who has been with me every step of

the way, supporting me throughout this journey for knowledge. Your support has meant everything to me. We started this journey together for knowledge, and your support has meant everything to me.

Dedication

A Mami, por enseñarme que todo se puede aprender.

A Papi, mi apoyo incondicional.

A Chen, por su amor y paciencia.

A Cristi, mi motivación final y mi mayor logro.

A Cairo, compañero fiel.

A mis hermanas Ana y Laura, y familia.

A Puerto Rico, mi bella isla que me formó.

Y a todos los que me apoyaron en este camino les dedico esta tesis.

Abstract

Permafrost, a critical carbon reservoir, is degrading under climate change, threatening to amplify global warming through carbon feedback. Traditional temperature driven models, which focus on heat diffusion, fail to adequately represent energy exchanges during phase transitions, a key driver of thaw processes. This thesis introduces a novel energy flow framework that directly models energy conservation, phase changes, and variable thermal properties. By prioritizing energy density as the core variable, rather than temperature, the framework captures the phase change more naturally. Through proof-of-concept simulations, we systematically analyze how geothermal heat flux and soil water content govern thaw rates. A pivotal finding is the non-linear relationship between water content and thaw timescales: permafrost with low ice content degrades orders of magnitude faster than ice-rich systems. The energy of fusion parameter emerges as a critical control on phase transitions. By integrating empirical data, this work provides policymakers actionable insights into regional vulnerabilities. The framework advances permafrost modeling by shifting focus from temperature trends to energy-driven processes, emphasizing that water content, not just warming magnitude, determines permafrost resilience. This refines climate projections and underscores the urgency of addressing permafrost thaw in mitigation strategies.

Contents

List of Tables

List of Figures

Chapter 1

Introduction

1.1 Permafrost: Definition and Significance

Permafrost, permanently frozen soil, is a vast reservoir of organic carbon accumulated over millennia in a cold environment that slows decomposition. Defined by soil taxonomists as material that remains at or below 0°C for two consecutive years or more, permafrost thickness ranges from one to over 1,000 meters. It consists of a mix of soil, organic matter, rock, and sand, often mixed with large ice blocks. Approximately one-quarter of the northern polar region has permafrost-affected soils (Figure 1.2). As climate change accelerates, both the seasonal thaw depth and spatial extent of these soils are changing significantly, risking the release of vast quantities of greenhouse gases that could exacerbate global warming.

Figure 1.1: Permafrost melting in the Arctic region of Svalbard. [1]

Figure 1.2: Latitudinal zonation of permafrost in the northern circumpolar region [2].

As the planet warms, permafrost thaws and degrades, releasing carbon dioxide, methane, and nitrous oxide into the atmosphere. These emissions originate from the degradation of preserved organic material in frozen soils, including the remains of plants, animals, and microbes that have resisted decomposition over millennia. The release of these greenhouse gases creates a positive feedback loop. Despite its critical role in the Earth system, the timeline of permafrost degradation remains poorly understood in the Earth system. The Intergovernmental Panel on Climate Change (IPCC) Sixth Assessment Report (AR6 [11]) has high confidence in ongoing permafrost thaw but low confidence in the timing and magnitude of emissions.

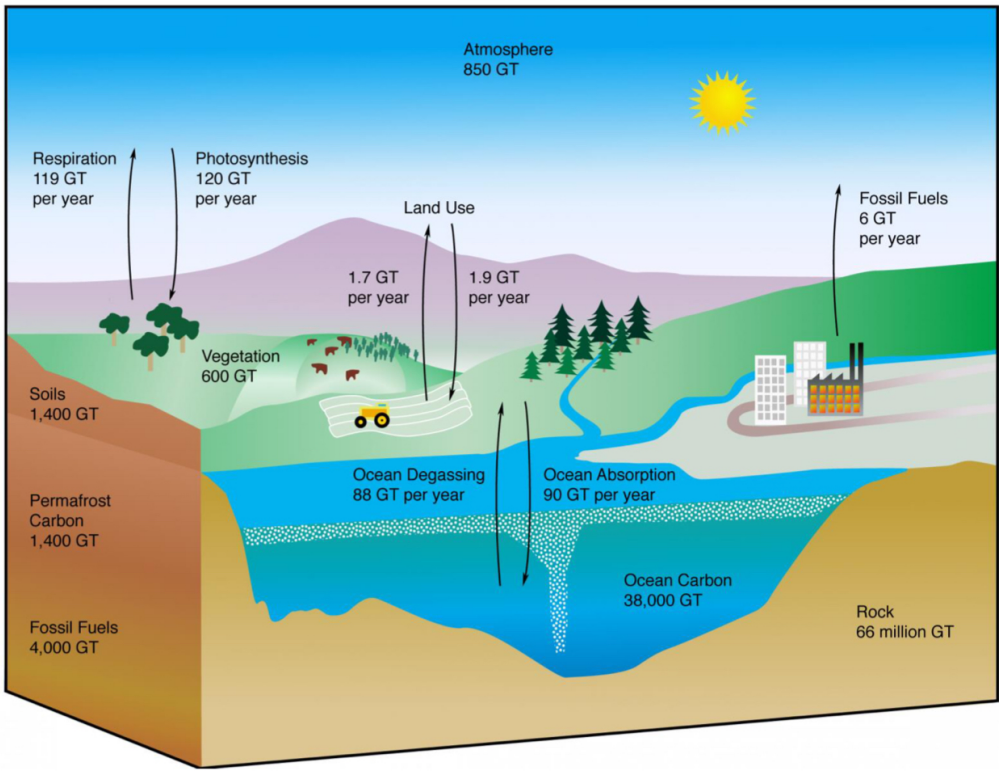

Figure 1.3: National Snow and Ice Data Center (NSIDC) diagram on the role of permafrost in the global carbon cycle. [3]

This uncertainty stems from variability in empirical and modeled estimates and limited representation of essential permafrost processes in Earth System Models (ESMs). For instance, only two of eleven ESMs in AR6 include permafrost carbon, often omitting important processes like abrupt thaw events, vegetation interactions, and wildfire dynamics [12].

1.2 Research Objectives and Thesis Organization

This thesis addresses gaps in permafrost dynamics modeling by introducing a conceptual framework rooted in energy principles. Current models insufficiently represent key physical processes such as phase transitions, latent heat effects, and complex thermal properties. The proposed approach provides an energy-based analysis of permafrost behavior under changing climatic conditions in the following chapters:

- **Chapter 2** introduces conceptual climate models, focusing on adaptations of the Budyko-Sellers framework to analyze permafrost recession and carbon feedback potential.
- **Chapter 3** examines localized thermal dynamics through Hill's heat diffusion model, exploring permafrost thaw progression and laying groundwork for more comprehensive approaches.
- **Chapter 4** reviews Sun et al.'s empirically parameterized model, incorporating thermal conductivity, heat capacity, and latent heat effects.

- **Chapter 5** develops the Energy Flow Model, explicitly integrating the energy of fusion to improve simulation accuracy of spatial and temporal thaw dynamics.

- **Chapter 6** investigates how variations in water content affect permafrost thaw rates, offering insights into degradation patterns and their implications for carbon release.

This unified mathematical framework bridges the gap between complex permafrost dynamics and their global implications, offering critical insights into one of the most significant yet understudied drivers of climate change.

Chapter 2

Conceptual Climate Models

2.1 Foundations of Energy Balance

A conceptual climate model is a simple representation of the Earth's climate system that captures essential processes. Unlike complex numerical models in climate science, which simulate the Earth's climate in great detail, conceptual models focus on specific relationships within the climate system. Conceptual climate models are valuable for researchers, educators, and policymakers, provide insights into mechanisms driving climate phenomena without computational complexity. These models study specific climate processes, test hypotheses, and communicate key concepts effectively to a broader audience. Despite their simplicity, they can offer valuable insights into the climate system's behavior under various conditions.

An example of a Conceptual Climate model is the Energy Balance Model (EBM). EBMs are simplified climate system models. Studying these models offers conceptual

tools for understanding climate change. They also are easier to understand from analytical and numerical perspectives. The main simplification is that they eliminate dependence on complex mechanisms such as the ocean circulation, wind, and Earth's rotation.

A primary advantage of conceptual models is their interpretability. Governed by large-scale physical mechanisms, they are more understandable and tractable than global circulation models. They also offer a theoretical understanding of climate phenomena. A notable example is the Budyko-Sellers Energy Balance Model [13], which examines how variations in solar radiation and surface reflectivity affect global temperature. This model is particularly useful for studying the ice-albedo feedback mechanism, where white ice reflects sunlight back to space, keeping Earth cool, while darker surfaces exposed by melting ice absorb more sunlight, leading to further warming and ice loss in a self-reinforcing cycle.

2.2 Budyko-Sellers Energy Balance Model

2.2.1 Preliminaries

The Budyko-Sellers energy balance model combines two influential climatology models proposed by Mikhail Budyko and Paul J. Sellers in the late 1960s. The aim of the model is to quantify the energy balance at the Earth's surface. Budyko developed a simplified energy balance model to study the long-term average climate conditions by balancing incoming solar radiation and outgoing longwave radiation.

It divides the Earth's surface into land and ocean components and assumes the climate tends toward equilibrium over time. Sellers [14] developed a model that independently addressed detailed processes and factors affecting energy balance. His model accounts for the atmosphere, land surface, and ocean, considering factors such as albedo, which is the standard measure of reflectivity of the Earth's surface, and the role of vegetation in influencing energy exchange, addressing the role of clouds, greenhouse gases, and heat storage in the ocean. This approach allows for a more dynamic climate representation compared to Budyko's simpler equilibrium model. The equations I will present pertain to what is known in the literature as the Budyko-Sellers Energy Balance Model. This integration combines elements from both Budyko's and Sellers' models. In summary, the Budyko-Sellers energy balance model is a synthesis of Budyko's equilibrium approach and Sellers' more detailed and dynamic model.

2.2.2 Governing Equations and Parameters

The model describes the latitudinal distribution of surface temperature T with a single dependent variable, emphasizing that the energy the Earth receives from the sun's radiation must balance the radiation the Earth loses to space by reemission and black-body radiation. The governing equation is given by the differential-integral equation:

$$R\frac{\partial T(y,t)}{\partial t} = (1-\alpha(y,\eta))Qs(y) - (A + BT(y,t)) + C(\bar{T}(t) - T(y,t)) \qquad (2.2.1)$$

Table 2.1: Variable and Parameter description for Budyko's model

Variable	**Value**	**Units**	**Description**
t	-	year	Time
y	-	-	Sine of Latitude
T(t,y)	-	°C	Surface Temperature
Parameter	**Value**	**Units**	**Description**
R	-	W s m^{-2} $°C^{-1}$	Planetary Heat Capacity [15]
Q	343	W m^{-2}	Insolation [16]
s_2	0.482	dimensionless	Obliquity effect on insolation [17]
A	202	W m^{-2}	Temperature-independent outgoing longwave radiation [16]
B	1.9	W m^{-2} $°C^{-1}$	Temperature-dependent outgoing longwave radiation [16]
C	3.04	W m^{-2} $°C^{-1}$	Heat transport coefficient
α_1	0.32	dimensionless	Albedo for latitudes south of ice line [16]

Continued on next page

Table 2.1 – continued from previous page

Variable	**Value**	**Units**	**Description**
α_2	0.62	dimensionless	Albedo for latitudes north of ice line [16]
T_c	-10	°C	Critical temperature at the ice boundary [16]
η	$\sin(72°)$	-	Sine of Latitude of the ice line [16]

The rate of change of Earth's surface temperature equals the net absorption of solar energy input minus the Earth's outward radiation, plus the heat gained or lost from transport. Related physical parameters are shown in table 2.1. These values are approximations, valid for the applications discussed. We assume symmetry about the equator, focusing only on the northern hemisphere. On the left-hand side of the equation, we have the constant R, a proportionality term for planetary heat capacity, and the partial derivative of T with respect to time. The value of R is important dynamically since it governs the rate at which the temperature responds to changes in the energy balance. First, we consider the incoming solar radiation on the right side. The incoming energy from the sun is input into the atmosphere and ocean system, denoted by constant value Q. This term is multiplied by $s(y)$, the distribution of insolation across latitudes. This function is normalized, with $y = \sin\theta$

and θ accounting for latitude. Sine is used because sunlight is not evenly distributed across the surface. We conventionally use an approximation due to North [18]:

$$s(y) \approx 1 - s_2(\frac{1}{2}(3y^2 - 1)) \tag{2.2.2}$$

Next, we assume that the Earth is not absorbing all this energy from the sun. The Earth's surface has parts that are reflective and parts that are not. We let α denote the surface reflectivity of the Earth: the albedo:

$$\alpha(y) = \begin{cases} \alpha_1 & y < \eta \quad \text{[ice]} \\ \alpha_2 & y > \eta \quad \text{[no ice]} \end{cases} \tag{2.2.3}$$

We denote η as the latitude of the snow line, so $T(\eta) = T_c$ where T_c is the temperature at the snow boundary, and the albedo is:

$$\alpha_0 = \alpha(\eta) = \frac{\alpha_1 + \alpha_2}{2} = 0.47 \tag{2.2.4}$$

2.2.3 Physical Interpretation of Model Components

The amount of energy we absorb or reflect on the Earth's surface varies depending on the surface composition. For example, we could consider a flat northern region without melted ice or a uniformly reflecting surface. As we move south, we have regions where the ice is melting, increasing absorption. Therefore, we let the albedo be spatially dependent, determined by the latitude. The idea is that for α_1, we

assume that you have a higher albedo if you are north of the latitude θ, where regions are covered by snow. If you are closer to the equator, the albedo is lower because more energy from the sun gets absorbed due to vegetation or water. The subsequent terms on the equation, namely the **A+BT**, account for outgoing longwave radiation, which is the amount of radiation trapped in the atmosphere. The parameter **A** is of interest since it is related to greenhouse gas effects on the climate system [15]. Adding carbon dioxide to the atmosphere decreases its emissivity, allowing less energy to escape to space. Hence, outgoing longwave radiation should vary inversely with CO_2. The last terms, $C(\bar{T}-T)$, correspond to heat transport. The $\bar{T}$ accounts for the global mean temperature, i.e., the average annual temperature of the Earth's surface:

$$\bar{T} = \int_0^1 T(y)dy \tag{2.2.5}$$

The heat transport terms are due to the second law of thermodynamics, which, in principle, places constraints upon the direction of heat transfer. In layman's terms, hot things always cool down and reach an equilibrium temperature. There is no spatial dependence in $\bar{T}$. The intuition is that if the temperature at a particular latitude is warmer than the global average, energy will be transported away from that latitude – and vice versa: if it's colder, energy will be transported toward that latitude. Even though heat transport is represented as a simple linear term in our model, heat transport is accomplished through complicated physical mechanisms. For example, a hurricane takes energy from the equatorial and mid-latitudes and

redistributes it as it moves north into the higher latitudes. Ocean currents and atmospheric currents also play the same role on a larger scale and are the main drivers of energy redistribution on the Earth's surface.

In the next section, we will discuss the work of Nguyen and Zebrowski [4]. They use an approximation to determine global mean temperature and permafrost line location changes. Using this new temperature distribution, they adapted Budyko's model to determine the new position of the permafrost line under scenarios that describe the state of climate under possible future conditions.

2.3 Application to Permafrost: Nguyen and Zebrowski's Approach

The study adapted an energy balance model to investigate greenhouse gas emissions resulting from permafrost melt and their interactions with sea ice-albedo feedback. It demonstrated that the combined feedback mechanisms could amplify system bistability and hysteresis, leading to more complex climate dynamics. By modifying the Budyko energy balance model, the work linked permafrost surface area loss to the northward retreat of the permafrost boundary as global temperatures rise. The approach quantified potential carbon emissions from thawing permafrost but highlighted the need for further integration with the Budyko-Widiasih [19] energy balance framework to better capture these interactions.

2.3.1 Mathematical Formulation of the Adapted Model

Adapting Budyko's energy balance model, Nguyen and Zebrowski modeled the permafrost line latitude θ_p as a function of global mean temperature T. The model estimates permafrost surface area loss using spherical geometry:

$$\Delta SA = 2\pi R^2(\sin\theta_{p,\text{final}} - \sin\theta_{p,\text{initial}}), \tag{2.3.1}$$

where R is the radius of the Earth, $\theta_{p,\text{initial}}$ is the initial latitude of the permafrost line (e.g., $61°N$), and $\theta_{p,\text{final}}$ is the latitude after warming.

The change in latitude $\Delta\theta_p$ is calculated as:

$$\Delta\theta_p = \arcsin(\Delta p), \tag{2.3.2}$$

where Δp is determined from the temperature-dependent shift in the sine of the latitude:

$$\Delta p = p'(T)\Delta T, \tag{2.3.3}$$

and $p'(T)$ is approximated by:

$$p'(T) = \frac{-C}{3Qs_2p(T)(1-\alpha_1)}, \tag{2.3.4}$$

where C is the heat transport coefficient, Q is the solar constant, s_2 is the effect of obliquity on insolation, and α_1 is the albedo for regions south of the snow line.

2.3.2 Carbon Emissions from Permafrost Thaw

The relationship between carbon emissions and surface area loss is modeled as:

$$\text{Carbon emissions} = \text{Total Carbon in Permafrost} \times \frac{\Delta SA}{\text{Original Permafrost Surface Area}}. \tag{2.3.5}$$

Given an initial permafrost area of approximately $1.32 \times 10^{13}\,\text{m}^2$ and a total carbon reservoir of 1,672 gigatons, the emissions are directly computed as:

$$\text{CO}_2 \text{ emissions} = \left(\frac{1672\,\text{Gt}}{1.32 \times 10^{13}\,\text{m}^2} \right) \times \Delta SA. \tag{2.3.6}$$

Nguyen and Zebrowski applied this model to several IPCC Fourth Assessment Report scenarios, including A1B, A2, and Paris Agreement scenarios (e.g., Paris A and Paris B), as well as an extreme $70^\circ N$ scenario. Their results showed that even optimistic scenarios like Paris A (limiting warming to $1.5^\circ C$) would lead to significant carbon emissions due to permafrost thaw.

2.3.3 Implications and Limitations

This work highlighted the strong positive feedback loop between rising global temperatures, permafrost melt, and carbon release. The combination of sea ice-albedo feedback and permafrost carbon feedback amplifies the climate response, increasing the risk of tipping points. However, the study used simplified assumptions, such as

assuming uniform carbon density.

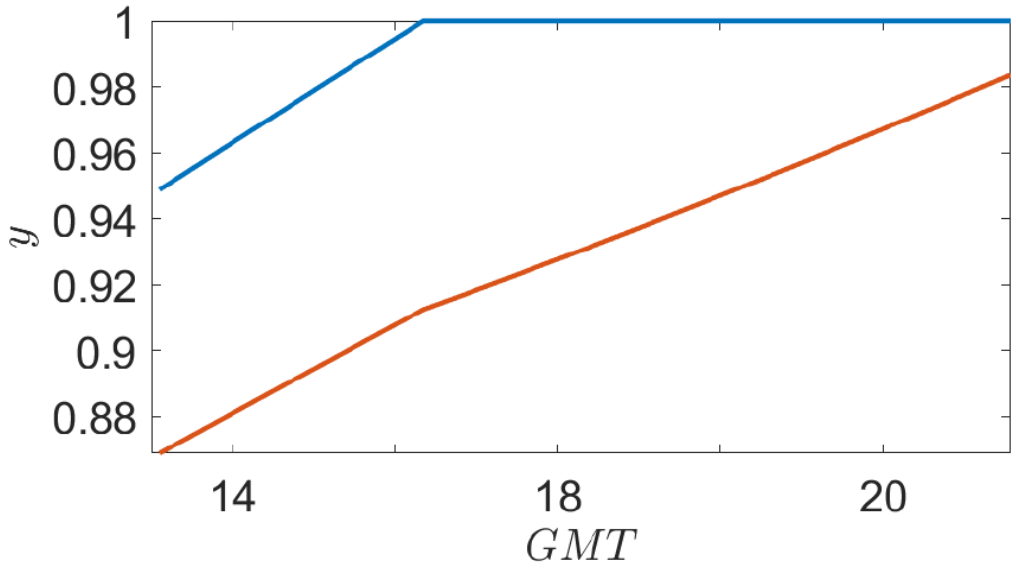

Figure 2.1: Equilibrium latitude of the snow line and permafrost line as a function of global mean temperature. The plot demonstrates how rising temperatures lead to the northward retreat of the permafrost line, emphasizing the strong feedback loop associated with carbon release from thawing permafrost (adapted from [4]).

Nguyen and Zebrowski's findings serve as a foundation for further research, including efforts to couple the permafrost model with the Budyko-Widiasih energy balance framework. Building on conceptual climate models, the next chapter examines localized thermal processes using Hill's heat diffusion model to explore permafrost thaw. While conceptual models offer valuable insights, their simplicity limits the ability to represent complex processes like phase transitions and latent heat effects. To address these gaps, later chapters transition to advanced numerical methods, incorporating empirically derived parameters, such as those from Sun et al., which enhance the representation of thermal conductivity, heat capacity, and latent heat.

Chapter 3

Simplified Heat Diffusion:

Insights into Thawing Dynamics

3.1 Fundamentals of Heat Transport in Frozen Ground

This chapter examines Hill's [6] conceptual model for permafrost thawing, which explores the dynamics surrounding explosive gas emissions and the formation of permafrost craters [5], phenomena increasingly prevalent amid ongoing climate change. Hill's approach employs a simple heat diffusion model to explore mathematical links between permafrost thaw and the explosive events observed during permafrost thaw, which involve a pressure buildup beneath the permafrost followed by sudden gas emission through the surface. The model demonstrates that the explosive behavior causing permafrost craters may be enable, in part, by heat diffusion processes

under specific parameter values and boundary conditions. By incorporating a linearly increasing surface temperature to mimic global warming, the model reveals a key finding: an asymmetric melting pattern characterized by faster thawing at the permafrost's lower boundary. This phenomenon, referred in the literature as *upward thawing* [9], could potentially explains the formation mechanism of permafrost craters. This asymmetric melting pattern may facilitate the accumulation of gas pressure, particularly in regions of continuous permafrost with high ice saturation. Consequently, it creates conditions conducive to sudden and explosive gas release, potentially leading to the observed crater formations.

3.1.1 Permafrost craters: Formation and significance

Permafrost craters, known as thermokarst, are geological features primarily found in regions with extensive permafrost in Siberia. These craters typically form due to the rapid thawing of ice-rich permafrost, causing surface material to collapse and create depressions. Due to their remote and inaccessible nature, the study of these craters largely relies on remote sensing techniques, particularly satellite imagery. Various sensors, including optical, thermal, and radar, provide valuable data for monitoring changes in permafrost landscapes over time.

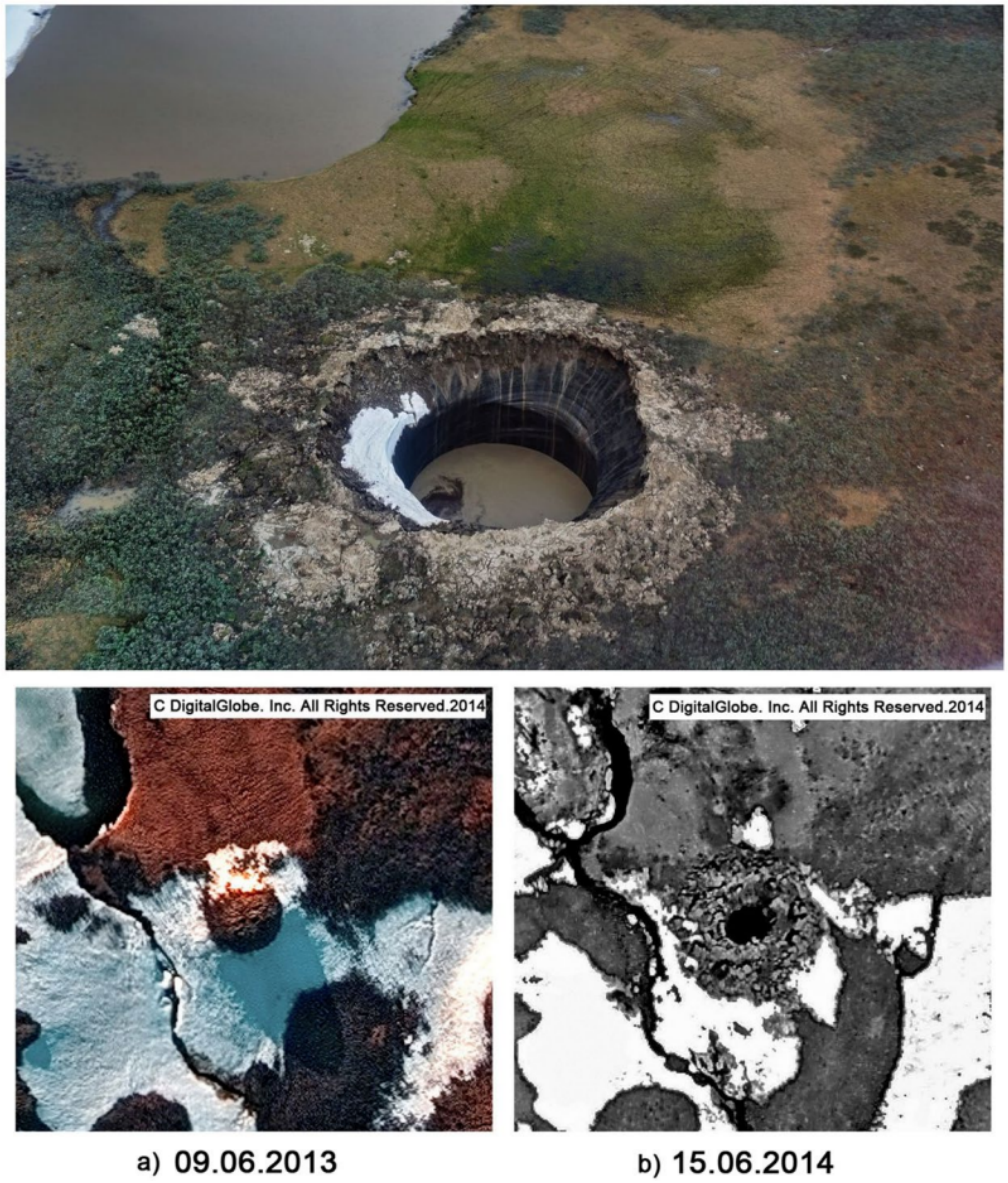

Figure 3.1: Yamal crater on July 15, 2015 (Photograph by Ruslan Amanzhurov) and high-resolution satellite imagery of 2013 (a) and 2014 (b). [5]

An explanation for the explosive behavior observed in permafrost crater formation emphasizes the role of pressure buildup due to gas release beneath the frozen

layer. For the permafrost crater in Figure 3.1, [5] propose a process of terrestrial cryovolcanism. This hypothesis involves freezing a sub-lake talik (an unfrozen layer within permafrost), pingo formation, and subsequent explosive release of pressurized gas and water. Permafrost contains significant amounts of trapped gases, including methane and carbon dioxide, released as the permafrost thaws. This process can lead to the formation of gas pockets beneath the surface, creating pressure within the permafrost layer. As this pressure builds up, it can weaken the overlying soil and ice layers. When the pressure exceeds the strength of the surrounding material, a sudden collapse can occur, resulting in crater formation. This process can be further exacerbated by increased temperatures, changes in precipitation patterns, and disturbances to the permafrost layer caused by human activities.

Acknowledging the limited mathematical studies on factors affecting crater formation, Hill [6] proposes a heat conduction-based model for permafrost melt. This model offers a simplified yet plausible explanation for the observed explosive behavior, highlighting the role of pressure buildup due to gas release beneath the permafrost layer.

It suggests that the complex dynamics of gas accumulation and release beneath the permafrost layer could be approximated using a basic diffusion equation, even without explicitly incorporating a pressure term.

3.2 Model Development and Implementation

The model describes heat conduction through a column of lithosphere, providing an idealized representation of permafrost melt compared to current, more complex models [20, 21]. Despite its simplicity, the model suggests that even basic processes may govern the sudden gas release, leading to explosive events similar to those observed in the Yamal Peninsula [5, 22]. The paper concludes with an overview of the model's behavior as temperature increases linearly and examines the likelihood of explosive gas liberation under specific conditions, particularly thin permafrost layers and high ice saturation [23].

The model illustrates the process of permafrost thawing in response to linear temperature increments. The initial assumptions delineate two distinct layers of permafrost: the active layer, which undergoes freezing and thawing cycles, and the permanently frozen layer. This conceptualization allows us to consider individual columns at various latitudes explicitly.

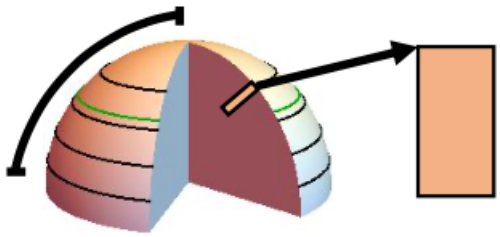

Figure 3.2: Hemispheric diagram depicting the attachment of column models across latitudes to simulate heat diffusion and climate dynamics [6].

3.2.1 Governing Equations and Boundary Conditions

At a given latitude y, $T_y(z,t)$ represents the temperature at depth z within the soil. We describe the vertical heat diffusion through the soil using a heat equation with Dirichlet boundary conditions. The lower boundary condition incorporates a constant heat source, M (representing the mantle), which accounts for Earth's internal energy and constitutes the heat influx from the permafrost base. Assuming equilibrium as the initial condition, Figure 3.3 depicts the column model along with its boundaries.

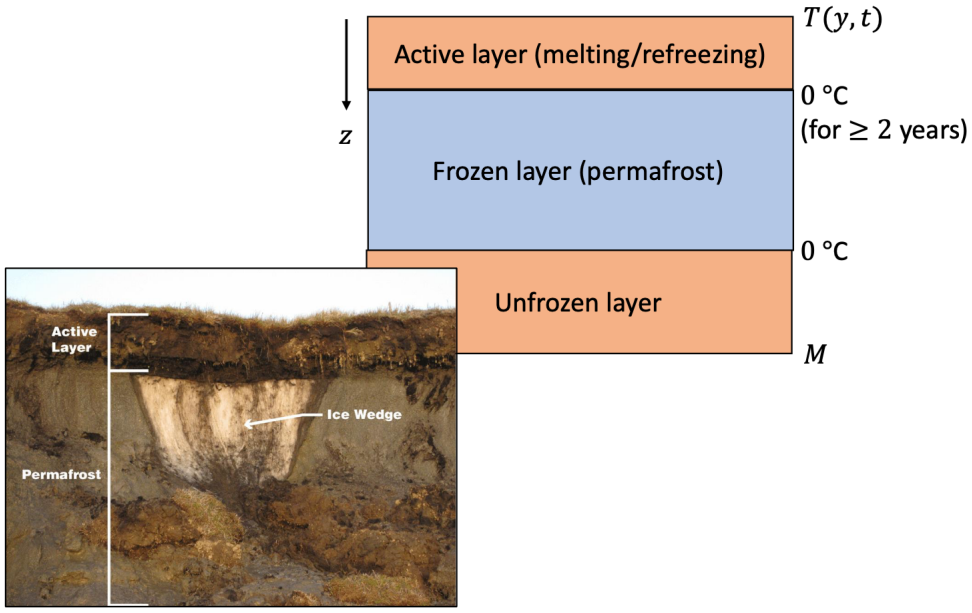

Figure 3.3: Column model for permafrost.

Thus, using the standard heat equation we have:

$$\frac{\partial T_y(z,t)}{\partial t} = k\frac{\partial^2 T_y(z,t)}{\partial z^2}, \quad t > 0, \quad 0 \leq z \leq l \tag{3.2.1}$$

At the surface boundary, two scenarios could be considered: one informed by Budyko's model,

$$T_y(0,t,y) = T(y,t) \tag{3.2.2}$$

and another, which we will refer to, is approximated using a sinusoidal fit,

$$T_y(0,t;y) = T_S(t) + F \tag{3.2.3}$$

It is important to note the difference in timescales: Budyko's model employs yearly averages, whereas the sinusoidal fit is based on daily averages. However, this model overlooks the heat required to melt permafrost, a significant factor considered by Sun [9] and in Chapter 5.

The approximation of surface temperature as a sinusoidal curve with a period of one year accounts for seasonality. This representation combines the surface temperature $T_S(t)$ with a constant forcing factor, representing a linear temperature rise. Derived from a permafrost line situated at 61° N and informed by yearly average temperature fluctuations, this fit is:

$$T_S(t) = -5 - 20\cos(2\pi t) \tag{3.2.4}$$

This periodic boundary condition effectively captures seasonal variations. Figure 3.4 juxtaposes this approximation with monthly mean land surface estimates from 1961 to 1990, chosen due to data availability. The data originates from CRU CLv2.0 [24].

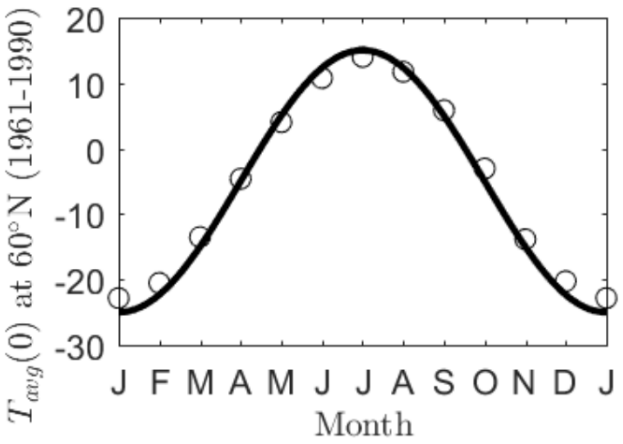

Figure 3.4: Boundary condition $T(y,t) = -5 - 20\cos(2\pi t)$, using fit from data: CRU CL v2.0. The sinusoidal curve represents the annual temperature cycle at 61°N latitude, capturing seasonal variations. Scatter points show actual monthly average temperature observations from 1961-1990.

At the lower boundary, we set:

$$T_y(l,t;y) = M \tag{3.2.5}$$

Our initial condition becomes:

$$T_y(z,0) = \frac{M - T(y,0)}{l} z + T(y,0) \tag{3.2.6}$$

3.2.2 Parameter Selection and Model Setup

The parameter k varies significantly depending on soil type: sandy, rocky, or organic, and its moisture content. Refer to the following table 3.2.2 for a list of parameter ranges. To simulate a thin layer of permafrost, the simulation we presents sets $M = 60$ which is out of the empirical range.

Variable/ Parameter	**Value**	**Units**	**Description**
z	-	m	Soil depth
l	1,000	m	Depth assumption [25]
M	[10,35]	C°	Heat source range from the convective portion of the mantle
M	60	C°	Heat source from the convective portion of the mantle used in simulation
k	[75,828]	C°	Thermal diffusivity range [26]
$k = \frac{K}{\rho c}$	700	C°	Thermal diffusivity used in simulation
ρc	0.5	$\frac{cal}{cm^3 K}$	Volumetric heat capacity of the medium [27]
K	[5,55]	$\frac{W}{mK}$	Thermal conductivity
F	0	C°	Temperature forcing

Although higher than the expected temperature at a depth of $1,000$ m, this value represents a thin permafrost layer without adding undue complexity to the model. The aim is to get a temperature profile similar to Figure 3.5.

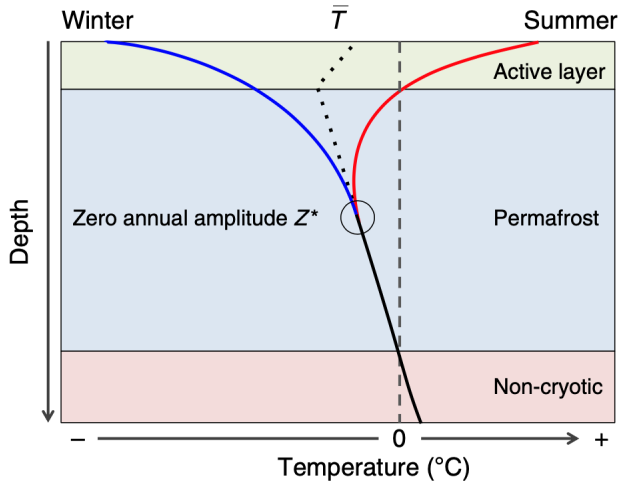

Figure 3.5: Schematic from [7] that shows the maximum (red line) and minimum ground temperature (blue line) during the year and how they converge to the mean annual temperature $\bar{T}$ at the depth at which seasonal changes in temperature are $\leq 0.1°C$, $Z^\star$. Black dots indicate the schematic mean temperature for permafrost soils. [7]

3.3 Analysis of Thawing Patterns and Crater Formation

Preliminary results occured on a reasonable timescale. Figure 3.6 shows temperature variation mid-simulation as F ramps linearly from 0°C to 3°C over 100 years, with maximum (red), minimum (blue), and average (black) temperatures at $t = 50$ years. This temperature profile is qualitatively similar to figure 3.5.

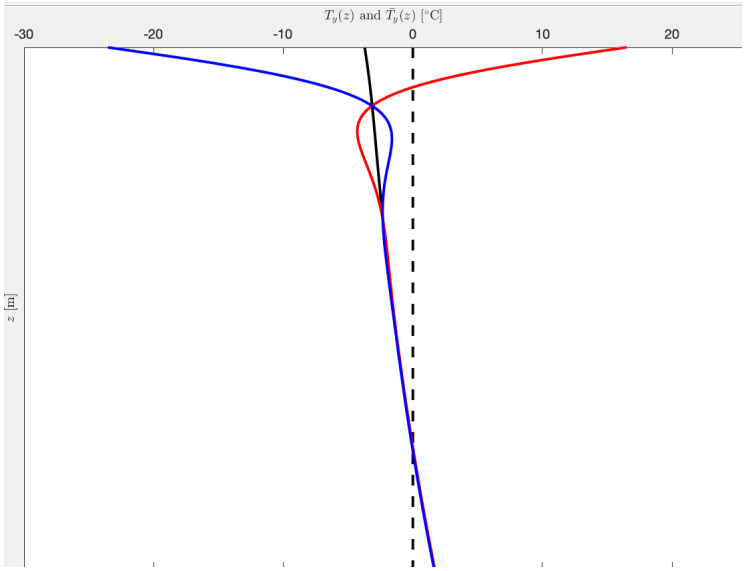

Figure 3.6: Temperature profile at year 50 of simulation that increased the parameter F linearly from 0°C to 3°C over 100 years. The horizontal axis is temperature in Celsius, and the vertical axis is soil depth in meters. It shows the maximum temperature in red, the minimum temperature in blue, and the average temperature in black. This profile reveals the presence of an active layer near the surface and the depth of the permafrost boundary. The figure is significant as it demonstrates the model's ability to reproduce key features of permafrost thermal regimes.

Although the model lacks the physics for a quantitatively accurate temperature profile, it provides a qualitatively similar one. A sensitivity analysis is needed since the chosen value $M = 60$ falls outside the observed parameter range but was selected to enable centennial-scale melting for the given parameters. The MATLAB solver `pdepe`, suitable for 1-D parabolic differential equations with slab symmetry, was used. Figure 3.7 shows temperature evolution over the simulation, with permafrost boundaries marked by the black curve. Permafrost begins above a thin active layer and ends at the mantle boundary M. Notably, increasing F alters the surface boundary, causing faster melting from the bottom than the top, consistent with

other models [9].

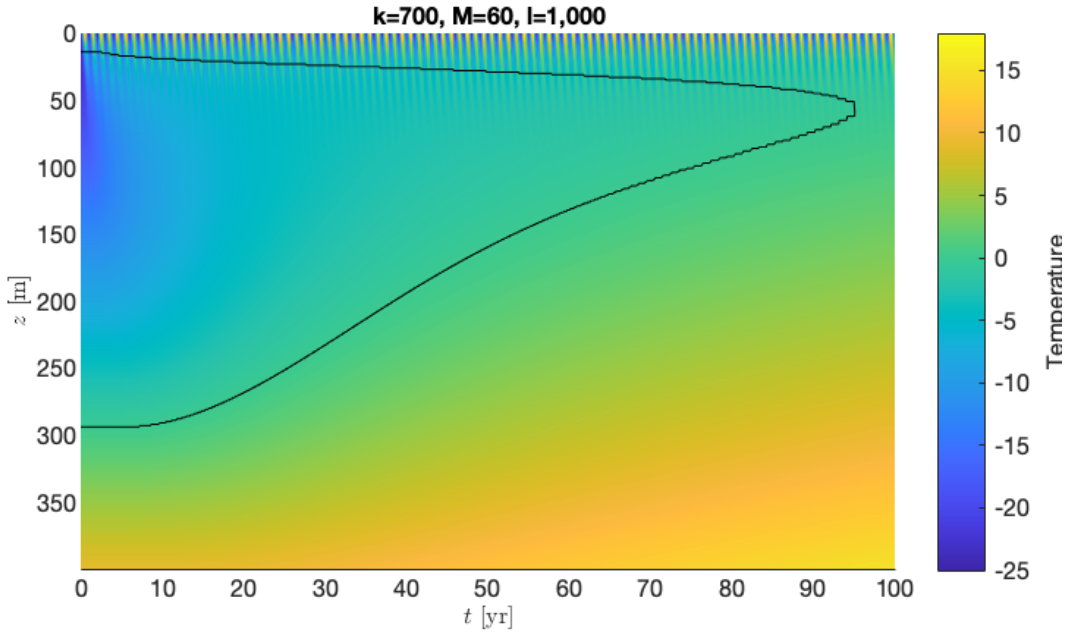

Figure 3.7: Permafrost depth variation over 100 years as F increases. The color gradient represents temperature, and the black line marks the permafrost boundary, highlighting faster melting at the lower boundary. This asymmetry is key to understanding the potential mechanism for gas pressure buildup and subsequent explosive release [6].

The model's results offer a compelling explanation for the formation of permafrost craters, consistent with observed phenomena. Figure 3.7 illustrates that as surface temperatures rise, the lower boundary of the permafrost experiences the initial and most significant thawing. This asymmetric melting pattern, characterized by faster thawing from below than above, could be the key to understanding the explosive nature of crater formation. As the lower permafrost boundary melts more rapidly, it potentially creates a reservoir where gases from thawing permafrost can accumulate. The upper permafrost layer, which remains largely frozen due to

slower surface melting, may act as a cap, trapping these gases and allowing pressure to build. It is to be noted that permafrost becomes nearly impermeable to methane at high saturation levels, further contributing to this pressure accumulation. When the pressure eventually exceeds the structural integrity of the overlying permafrost, it may lead to a sudden and explosive release through the weakest point. This mechanism aligns well with field observations of permafrost craters, which show evidence of violent eruptions that eject ice and soil debris. Therefore, the model's demonstration of preferential bottom-up melting establishes a critical connection between the heat diffusion process and the observed explosive formation of permafrost craters in nature.

Hill's simplified heat diffusion model provides valuable insights into permafrost thaw dynamics, but it's important to contrast its results with those of more complex models and acknowledge its limitations. More complex models, such as the Community Land Model (CLM) by Lawrence [28], the GIPL 2.0 model by Marchenko [29], and the Cryogrid 3 model by Westermann [30], incorporate additional physical processes not captured in Hill's model. These include detailed soil physics, hydrology, biogeochemistry, latent heat effects, phase changes, varying thermal properties, surface energy balance, and snow cover. As a result, these models often predict more gradual thawing processes and less pronounced bottom-up thawing compared to Hill's results.

Hill's model doesn't account for several important factors: the latent heat of fusion, soil heterogeneity, water content changes and phase transitions, gas dynamics, seasonal active layer dynamics, three-dimensional effects, biological processes, and complex climate feedbacks. These omissions may lead to overestimation of thawing rates and simplification of real-world permafrost behavior. Despite these limitations, Hill's model aligns with more complex models in predicting the increased vulnerability of permafrost to thawing under warming scenarios. The simplicity of Hill's approach allows for a clear illustration of key processes, while more complex models offer greater precision at the cost of increased computational demands and parameter uncertainties.

3.4 Alternative Mechanism: Osmotic Pressure and Crater Formation

Recent findings reported by the American Geophysical Union [8] highlight a mechanism explaining the mysterious crater formations in Siberian permafrost, based on research by Morgado et al [31]. This mechanism suggests that osmotic pressure, rather than just thermal effects, plays a crucial role in the explosive formation of these craters.

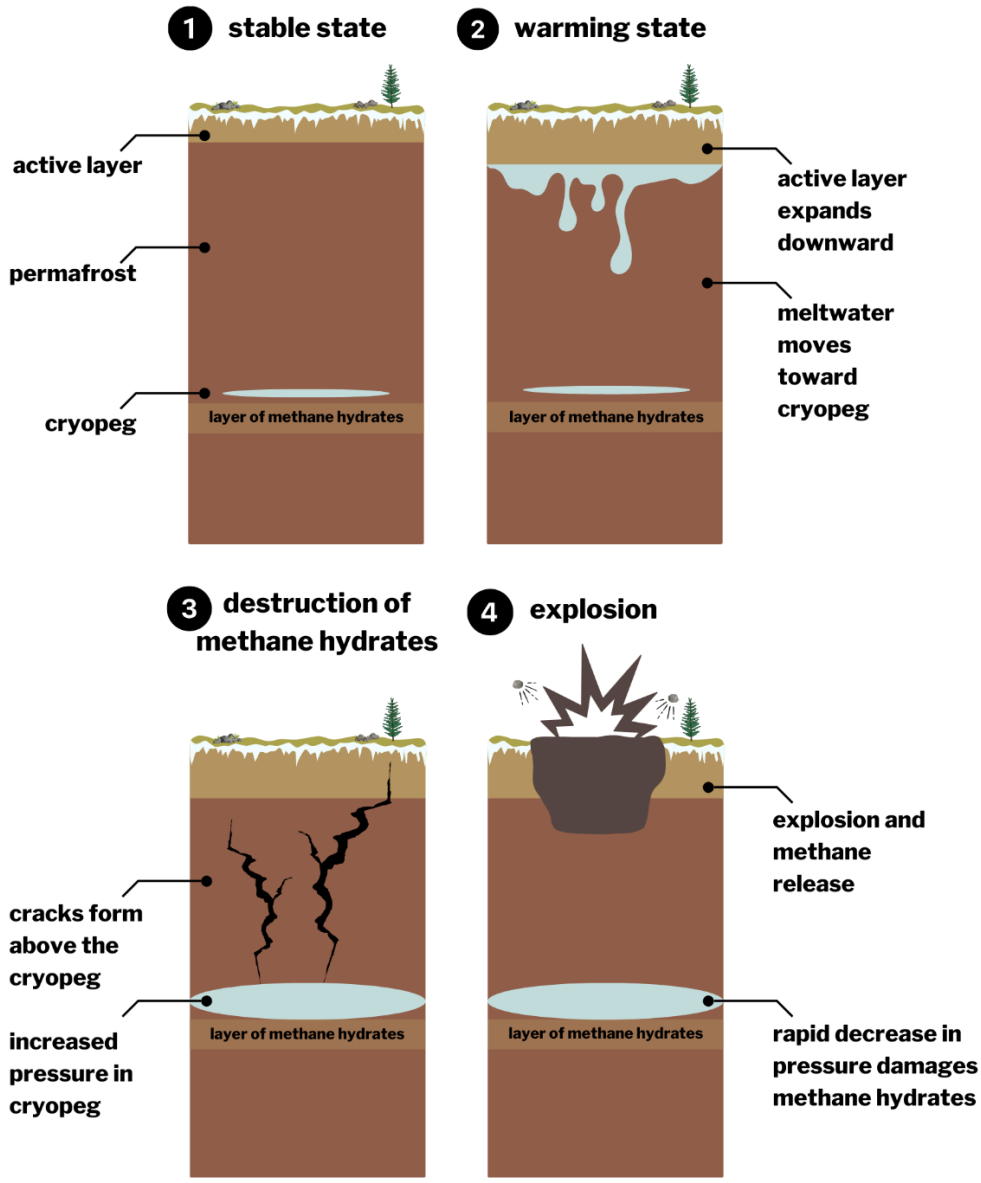

Figure 3.8: Schematic showing the process of permafrost crater formation: (1) Climate warming causes melting in the active layer, (2) Meltwater migrates to the cryopeg through osmosis, (3) Cryopeg expansion leads to permafrost cracking, and (4) Surface breach triggers rapid depressurization and methane hydrate decomposition. Credit: AGU/Madeline Reinsel [8].

The process begins with climate warming increasing the active layer depth, allowing more surface meltwater to penetrate the permafrost. This water is drawn downward by osmotic pressure toward cryopegs - lenses of highly saline unfrozen water found deep within the permafrost. As water accumulates in these cryopegs, they expand, creating pressure that can crack the surrounding frozen ground. When these cracks reach the surface, the sudden pressure release destabilizes methane hydrates below, triggering explosive events that form the observed craters.

This mechanism helps explain both the timing and explosive nature of crater formation, suggesting these events might become more frequent as climate warming continues to deepen the active layer. The process operates on decadal rather than millennial timescales, with pressure buildup occurring within years once conditions are suitable.

The combination of Hill's heat diffusion model and Morgado's osmotic pressure mechanism reveals the complex interplay between thermal and mechanical processes in permafrost crater formation. While these models provide valuable insights into explosive gas emissions and crater development, they simplify critical physical processes such as phase transitions and latent heat effects. To address these limitations, we next examine Sun et al.'s more comprehensive approach, which incorporates the crucial role of phase changes and varying thermal properties in permafrost thaw dynamics.

Chapter 4

Upward Thawing and a Phase-Differentiated Model

4.1 Preliminaries

Building upon the heat diffusion and osmotic pressure mechanisms discussed previously, we now examine a more comprehensive approach developed by Sun et al. [9]. Their model incorporates several crucial factors previously simplified: the latent heat of phase changes, depth-varying thermal properties, and long-term climate change effects. Additionally, their work accounts for distinct volumetric heat capacities and thermal conductivities in a piecewise linear manner.

4.2 Upward thawing

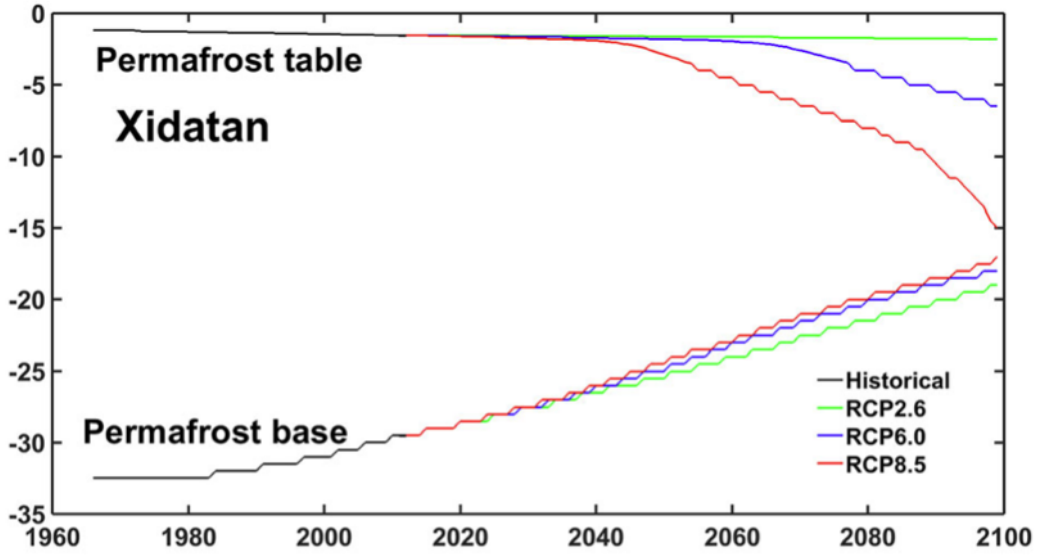

Figure 4.1: Simulation of permafrost evolution from 1966 to 2100, showing changes in the permafrost table and base at studied borehole sites under various RCP scenarios [9]

The evolution of mountain permafrost conditions at Xidatan in the Qinghai–Tibetan plateau, illustrated in Figure 4.1, demonstrates significant permafrost degradation from 1966 to 2100. Initially stable at around 32.5 m depth until the early 1980s, the permafrost base began a steady upward progression, reaching approximately 29.5 m by 2012. The model projects this trend to continue under all future climate scenarios, with the permafrost base potentially rising to as high as 17 m by 2100 under the most extreme warming scenario (RCP 8.5). This vulnerability is particularly pronounced in regions like Xidatan where the permafrost is relatively warm and thin.

4.3 Model Overview

4.3.1 Governing Equations

The one-dimensional numerical heat conduction model incorporates phase change, varying thermal properties with depth, and geothermal heat flux:

$$c_{\text{eff}}\frac{\partial T}{\partial t} = \frac{\partial}{\partial z}\left(\lambda\frac{\partial T}{\partial z}\right) \tag{4.3.1}$$

where c_{eff} is the effective volumetric heat capacity, λ is the thermal conductivity, T is temperature, t is time, and z is depth.

The model accounts for phase transitions through a piecewise definition of effective volumetric heat capacity:

$$c_{\text{eff}}(T) = \begin{cases} c_f, & T \leq T_1 \\ \frac{L(\theta-\theta_u)}{T_2-T_1} + \frac{c_f+c_u}{2}, & T_1 < T < T_2 \\ c_u, & T \geq T_2 \end{cases} \tag{4.3.2}$$

where c_f and c_u are the volumetric heat capacities of frozen and thawed soil respectively, L is the volumetric latent heat of phase change, θ is the total volumetric water content, θ_u is the volumetric unfrozen water content in frozen soil, and T_1 and T_2 are the boundaries of the phase transition interval temperature.

Similarly, the thermal conductivity varies between frozen and thawed states:

$$\lambda(T) = \begin{cases} \lambda_f, & T \leq T_1 \\ \lambda_f + \frac{\lambda_u - \lambda_f}{T_2 - T_1}(T - T_1), & T_1 < T < T_2 \\ \lambda_u, & T \geq T_2 \end{cases} \tag{4.3.3}$$

where λ_f and λ_u are the thermal conductivities of frozen and thawed soil respectively.

4.3.2 Boundary Conditions and Climate Scenarios

The upper boundary condition incorporates historical ground surface temperature (GST) and future climate scenarios:

$$T = T_0 + \frac{Gt}{365} + A \sin\left(\frac{2\pi}{365}t + \phi\right) \tag{4.3.4}$$

where T_0 is the initial annual mean temperature, G is the GST change rate, A is the GST annual amplitude, and ϕ is the initial phase angle aligning seasonal temperature patterns. The lower boundary condition at 100 meters depth uses a Neumann condition to represent geothermal heat flux.

Model calibration and validation drew from extensive field data collected at the Xidatan and Tanggula stations, including continuous monitoring data since 2005, borehole temperature measurements, and soil samples. Historical temperature records from nearby meteorological stations extended the dataset back to 1966,

while future projections incorporated various RCP scenarios. The model validation process compared simulated results with field measurements, ensuring accurate representation of both historical conditions and future projections across different climate scenarios.

Sun et al.'s model enhances previous approaches through two key improvements: a variable spatial resolution that optimizes computational efficiency while maintaining accuracy near the surface, and site-specific geothermal heat flux as a lower boundary condition for more realistic heat transfer representation at the permafrost base. This comprehensive treatment of thermal properties and phase changes provides the foundation for our energy-based modeling framework presented in the next chapter.

Chapter 5

Energy Flow Framework

5.1 Energy as the Fundamental Variable

This chapter presents a new method for modeling permafrost dynamics that employs energy instead of temperature as its key variable. Energy is crucial for understanding phase transition dynamics. The energy of fusion, heat absorbed during thawing or released during freezing, functions as a thermal buffer, significantly affecting permafrost's response to climate change. This buffering effect is evident in phenomena like the *zero curtain* [32], Figure 5.1, where soil temperature stays near 0°C during phase transitions due to energy absorption or release without temperature change. Traditional modeling approaches, such as the Stefan problem, treat transitions between frozen and thawed states as sharp boundaries.

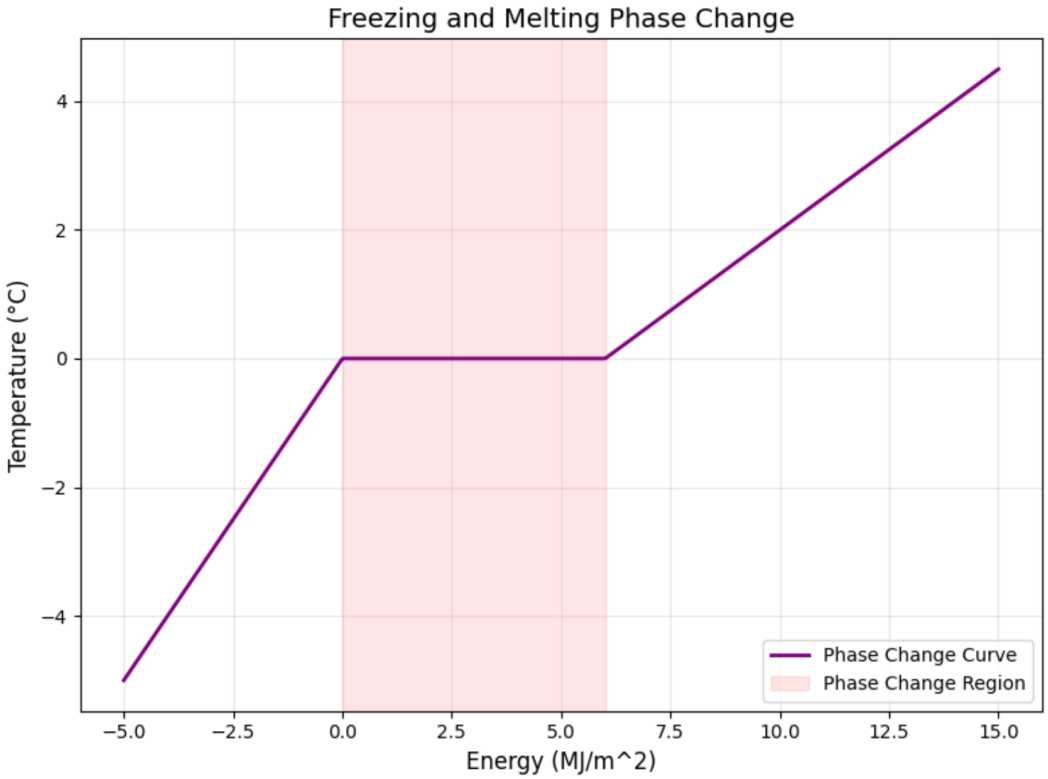

Figure 5.1: Temperature dependence on energy ilustrating the zero curtain.

Although mathematically appealing, this method necessitates tracking discrete interfaces and often depends on oversimplified material property assumptions. In contrast, real permafrost systems demonstrate gradual phase transitions, variable thermal properties, and complex environmental interactions that challenge these simplifications [21].

Our energy-based framework addresses these limitations. By utilizing energy density, we model phase transitions, account for latent heat via the energy of fusion parameter, and allow thermal properties to vary with the system's energy state. As soil moisture content varies, it creates heterogeneity in thaw rates and active

layer depth effects our energy formulation captures through their influence on the energy state. The resulting model offers a realistic framework integrating heat transfer, phase changes, and environmental conditions. This chapter details the mathematical foundations of this approach and demonstrates its comprehensiveness in understanding permafrost dynamics under climate change.

5.2 Evolution of Permafrost Modeling Approaches

5.2.1 From Stefan Problems to Modern Methods

Understanding permafrost dynamics requires robust models that capture the thermal and hydrological processes driving thaw and active layer evolution. Theoretical approaches to permafrost modeling have evolved significantly, incorporating physical principles to simulate heat transfer, phase changes, and feedback mechanisms within frozen ground.

A key aspect of modeling permafrost involves simulating the movement of the thaw front, where frozen soil transitions to a thawed state. Early models often relied on phase change frameworks similar to the Stefan problem, a classical mathematical approach to heat transfer during phase transitions [33]. These models excel at describing the latent heat effects and sharp phase boundaries associated with freezing and thawing processes [34, 21, 35]. However, the complexity of real-world permafrost dynamics—marked by heterogeneous soils, variable moisture, and non-linear heat transfer—has prompted the use of alternative approaches.

Modern permafrost models extend beyond the classical Stefan framework to address the coupled thermal, hydrological, and mechanical processes affecting permafrost. Painter [36] proposed an integrated model combining surface and subsurface thermal hydrology, emphasizing the role of water movement and its impact on heat transfer. Similarly, Walvoord and Kurylyk [37] reviewed how thawing permafrost alters hydrological pathways, calling for coupled models that link heat and water flow. These efforts underscore the need for new approaches that account for feedback mechanisms between thermal and hydrological processes.

CryoGrid 3, developed by Westermann [30], exemplifies this shift toward comprehensive modeling. This model simulates permafrost thermal regimes and thaw dynamics by incorporating heat conduction, phase changes, and ground subsidence due to ice melt. It effectively captures the interplay between latent heat effects, soil properties, and subsurface processes, enabling a nuanced understanding of permafrost behavior under changing climatic conditions.

5.2.2 The Role of Energy in Permafrost Thawing

Energy dynamics, particularly the role of latent heat during phase changes, are central to permafrost thaw modeling [38]. Latent heat reduces sensitivity to short-term temperature fluctuations [30]. Variability in soil moisture content amplifies this effect, leading to spatial heterogeneity in thaw rates and active layer depth [39]. Additionally, as thaw progresses, latent heat effects can create feedback loops, accelerating thaw in adjacent areas through increased water movement and heat

transfer [40].

Recent models have incorporated these complex energy effects to improve permafrost simulations. For instance, Nicolsky [34] developed a model that explicitly considers latent heat dynamics to predict long-term permafrost degradation. Such efforts highlight the importance of energy-driven processes in shaping permafrost systems.

These developments in permafrost modeling highlight that phase transitions, latent heat effects, and varying material properties all fundamentally relate to energy rather than temperature. This motivates our development of an Energy Flow framework that directly tracks the flow and storage of energy through the permafrost system.

5.3 The Energy Flow Framework

5.3.1 Variables, Material Properties, and Lower Boundary Considerations

The Energy Flow framework represents permafrost as a system where energy moves between phases and across spatial boundaries. While traditional models track temperature and must handle discontinuities during phase transitions, our approach uses energy density as the fundamental variable. This allows us to directly model phase changes and heat transfer through continuous variations in energy content, naturally accommodating the transitions between frozen and thawed states. The

framework's state is described by three primary variables: energy density $E(z,t)$ $[\frac{MJ}{m^3}]$, energy flux $q(z,t)$ $[\frac{MW}{m^2}]$, and temperature $T(z,t)$ [°C], varying over depth z [m] and time t [s]. Table 5.1 provides a complete overview of these variables and the associated material parameters.

Table 5.1: Variables and Parameters in Permafrost Modeling.

Symbol	**Type**	**Description**	**Units**
z	Variable	Depth	m
t	Variable	Time	s
$E(z,t)$	Variable	Energy density	$\frac{MJ}{m^3}$
$q(z,t)$	Variable	Energy flux	$\frac{W}{m^2}$
$T(z,t)$	Variable	Temperature	°C
E_{fus}	Parameter	Energy of fusion	$\frac{MJ}{m^3}$
β_{sol}	Parameter	Reciprocal of specific heat (solid)	$\frac{Km^3}{MJ}$
β_{liq}	Parameter	Reciprocal of specific heat (liquid)	$\frac{Km^3}{MJ}$
κ_{sol}	Parameter	Thermal conductivity (solid)	$\frac{MW}{mK}$
κ_{liq}	Parameter	Thermal conductivity (liquid)	$\frac{MW}{mK}$

Boundary Condition Formulation: Unlike traditional models that impose a fixed temperature at depth (Dirichlet condition), our Neumann formulation ($q(M,t) = \eta$) explicitly incorporates geothermal heat flux. Geological surveys document significant spatial variability in geothermal flux across permafrost regions [27]. By

prioritizing energy flux over fixed temperature at the lower boundary, the framework aligns with empirical data. The boundary choice, interacting with the soil's inherent material properties, directly regulate thaw patterns and energy redistribution.

The relationship between these variables is governed by material properties that characterize heat flow through permafrost. These properties differ between frozen and thawed states:

- Thermal conductivity (κ): Governs the rate of heat transfer through the soil
  - κ_{sol}: Thermal conductivity in the solid (frozen) state
  - κ_{liq}: Thermal conductivity in the liquid (thawed) state
- Inverse of volumetric heat capacity (β): Determines the soil's temperature response to heat input
  - β_{sol}: Inverse of volumetric heat capacity in the solid state
  - β_{liq}: Inverse of volumetric heat capacity in the liquid state
- Energy of fusion (E_{fus}): Quantifies the energy required for phase transitions

These parameters enable us to characterize the soil's thermal behavior over time and depth, including the energy required for permafrost thawing. The distinction between solid and liquid states for κ and β allows us to accurately represent the different thermal behaviors of frozen and thawed soil.

5.3.2 Energy Flow System

Our Energy Flow system consists of three coupled equations describing energy conservation, energy-temperature relationships, and energy transport, complemented by appropriate boundary conditions.

The system is described as:

$$\begin{aligned} \frac{\partial E}{\partial t} &= \frac{\partial q}{\partial z}, \\ T &= \Theta(E), \\ q &= \kappa(E)\frac{\partial T}{\partial z} \end{aligned} \tag{5.3.1}$$

These equations can be combined into a partial differential equation:

$$\frac{\partial E}{\partial t} = \frac{\partial}{\partial z}(\kappa(E)\frac{\partial}{\partial z}\Theta(E)). \tag{5.3.2}$$

The first equation in 5.3.2 embodies energy conservation, expressing that the rate of change of energy density equals the gradient of energy flow. The second equation in 5.3.2 establishes the relationship between temperature and energy density through the function $\Theta(E)$, while the third equation in 5.3.2 describes energy transport through the medium.

The system is completed by boundary conditions:

$$T(0,t) = T_0(t), \quad q(M,t) = \eta \tag{5.3.3}$$

where $T_0(t)$ represents surface temperature and η denotes geothermal heat flux at depth M. The boundary conditions expressed in terms of the energy variable E are:

$$E(0,t) = \Theta^{-1}(T_0(t)), \quad \kappa(E(M,t)) \cdot \left.\frac{\partial \Theta(E)}{\partial z}\right|_{z=M} = \eta \tag{5.3.4}$$

where Θ^{-1} is the inverse function that maps temperature to energy density. This combination of a Dirichlet condition at the surface and a Neumann condition at depth differs from traditional temperature-based approaches. Employing energy flux as a boundary condition at depth, rather than a fixed temperature, better aligns with the physical reality of geothermal heating processes. This distinction is particularly significant in light of geological evidence indicating substantial melting occurs from below in permafrost systems. Geologists have measured and modeled this heat flux for decades, consistently demonstrating its critical role in initiating and sustaining thawing processes at depth. Therefore, incorporating a heat-flow boundary condition is not merely a theoretical improvement but a practical necessity for accurately reflecting the dynamics of permafrost degradation[34] [41] [27]. Furthermore, this choice ensures that the model remains consistent with empirical observations of geothermal heating. A constant temperature assumption at depth would oversimplify these variations, potentially misrepresenting the rate and spatial heterogeneity of permafrost thaw.

The relationship between temperature and energy density is given by:

$$T \equiv \Theta(E) = \begin{cases} \beta_{sol} E, & E \leq 0, \\ 0, & 0 \leq E \leq E_{fus}, \\ \beta_{liq}(E - E_{fus}), & E_{fus} \leq E, \end{cases} \tag{5.3.5}$$

where β_{sol} and β_{liq} are the reciprocals of volumetric heat capacity in solid and liquid phases respectively, and E_{fus} is the energy of fusion. This piecewise definition naturally captures phase transitions, a crucial aspect in permafrost modeling where materials can exist in solid, liquid, or mixed phases.

The thermal conductivity varies with energy state according to:

$$\kappa(E) = \begin{cases} \kappa_{sol}, & E \leq 0, \\ \frac{\kappa_{sol}(E_{fus} - E) + \kappa_{liq} E}{E_{fus}}, & 0 \leq E \leq E_{fus}, \\ \kappa_{liq}, & E_{fus} \leq E, \end{cases} \tag{5.3.6}$$

where κ_{sol} and κ_{liq} are the thermal conductivities of the solid and liquid phases. This energy-dependent formulation accounts for varying thermal properties across different phases, enabling accurate representation of heat transfer in multi-phase permafrost systems.

The surface boundary temperature $T_0(t)$ is approximated by a sinusoidal curve

representing average temperatures at a given latitude. In contrast, the bottom boundary condition η represents the relatively stable geothermal heat flux from Earth's interior.

5.4 Numerical Implementation

To transform our continuous Energy Flow system into a computationally tractable form, we must develop a discrete representation that preserves the essential physics while enabling efficient numerical solutions. We establish conservation principles in discrete form, then detail our spatial discretization strategy, and finally present the complete numerical algorithm.

5.4.1 Conservation Laws in Discrete Form

Consider a volume with cross-sectional area A and height $\Delta z = z_2 - z_1$ within our permafrost column. The change in total energy within this volume over a time interval $\Delta t = t_2 - t_1$ is given by:

$$A\Delta z(E(t_2) - E(t_1)). \tag{5.4.1}$$

This change results from the net energy flux through the volume's boundaries. Energy enters through the upper boundary (z_2) at a rate Aq_2 and leaves through the lower boundary (z_1) at a rate Aq_1, giving the energy balance:

$$A\Delta z(E(t_2) - E(t_1)) = A(q_2 - q_1)\Delta t. \tag{5.4.2}$$

Rearranging and taking the limit as $\Delta t, \Delta z \to 0$ yields our fundamental conservation law:

$$\frac{\partial E}{\partial t} = \frac{\partial q}{\partial z} \tag{5.4.3}$$

This conservation principle forms the basis for our numerical discretization strategy.

5.4.2 Spatial Discretization Strategy

We model permafrost as a vertical column with cross-sectional area A and depth M, focusing on vertical heat transfer processes. Figure 5.2 illustrates our discretization scheme, which employs a staggered grid to represent energy and temperature variables accurately.

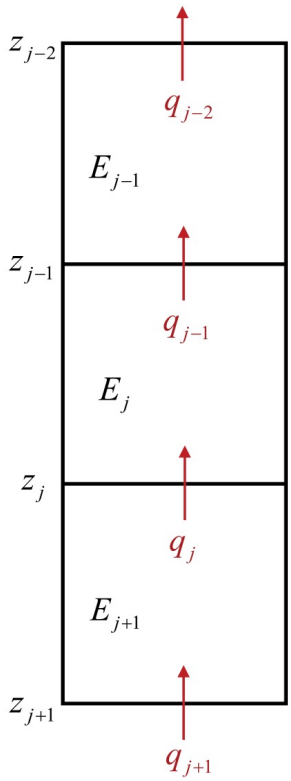

Figure 5.2: Discretization of the permafrost column showing where energy density E_j is defined, and energy flux q_j is computed. The vertical spacing Δz is chosen to balance resolution and computational efficiency.

The spatial domain $[0, M]$ is divided into n segments of height $\Delta z = M/n$, with grid points:

$$z_j = j\Delta z, \quad j = 0, 1, \ldots, n \tag{5.4.4}$$

At each grid point, we track the energy density $E_j(t)$ and temperature $T_j(t)$. The energy flux $q_j(t)$ is computed at the interfaces between segments at z_j, representing flow from segment $[z_j, z_{j+1}]$ into segment $[z_{j-1}, z_j]$. This staggered arrangement

naturally preserves energy conservation and handles the discontinuities at phase boundaries.

The total energy in each segment is:

$$H_{total,j}(t) = A \cdot \Delta z \cdot E_j(t) \tag{5.4.5}$$

The rate of change of total energy follows from our conservation principle:

$$\frac{dH_{tot,j}}{dt}(t) = A(q_j(t) - q_{j-1}(t)) \tag{5.4.6}$$

Combining these equations yields our fundamental discrete evolution equation:

$$\frac{dE_j}{dt} = \frac{q_j - q_{j-1}}{\Delta z}, \quad j = 1, 2, \ldots, n. \tag{5.4.7}$$

This discretization transforms our continuous Energy Flow system into a system of coupled ordinary differential equations while preserving the essential physics of energy conservation and phase transitions.

5.4.3 Numerical Algorithm

The discretized Energy Flow system 5.4.7 is solved by treating $E = (E_1, E_2, \ldots, E_n)$ in $\mathbb{R}^n$ as our primary variable and formulating the evolution as a vector field:

$$\frac{dE}{dt} = f(E). \tag{5.4.8}$$

The algorithm proceeds iteratively through the following steps:

1. Compute temperatures from energy densities using the phase transition function:

$$T_j = \Theta(E_j), \quad j = 1, 2, \ldots, n \tag{5.4.9}$$

2. Calculate effective thermal conductivities at segment interfaces:

$$\kappa_j = \begin{cases} \kappa(E_1), & j = 0 \\ \frac{\kappa(E_j)+\kappa(E_{j+1})}{2}, & 1 \leq j \leq n-1 \end{cases} \tag{5.4.10}$$

3. Evaluate energy fluxes between segments:

$$q_j = \begin{cases} \kappa_0 \frac{T_1 - T_0}{\Delta z/2}, & j = 0 \\ \kappa_j \frac{T_{j+1} - T_j}{\Delta z}, & 1 \leq j \leq n-1 \\ \eta, & j = n \end{cases} \tag{5.4.11}$$

4. Construct the complete vector field:

$$f_j(E) = \frac{q_j - q_{j-1}}{\Delta z}, \quad j = 1, 2, \ldots, n \tag{5.4.12}$$

The resulting system is numerically solved using Python. See the appendix for the code. The numerical implementation employs finite difference methods with

an explicit time-stepping scheme to solve the heat equation with phase transitions. The code tracks energy content and temperature separately through functions that handle phase transitions, temperature-dependent thermal properties, and energy content updates at each timestep. This approach captures the key physical processes of latent heat effects and seasonal temperature variations at the surface boundary over the simulation period.

Special consideration is given to the treatment of phase transitions, where the energy-temperature relationship is nonlinear. The algorithm handles these transitions naturally through the piecewise definitions of $\Theta(E)$ and $\kappa(E)$, ensuring accurate representation of the physics while maintaining numerical stability.

The numerical parameters, including spatial discretization Δz and temporal step size, are chosen to balance accuracy and computational efficiency. A detailed analysis of the numerical stability and parameter selection is presented in Chapter 6.

This numerical implementation enables us to simulate permafrost evolution over long time periods while accurately capturing the complex interplay between heat conduction, phase changes, and varying thermal properties throughout the soil column.

Chapter 6

Permafrost Response to Variable Water Content: Analysis Through Energy of Fusion

6.1 Parameter Selection and Validation

Our simulations use parameters chosen to enable comparison with Hill's temperature-based model while examining the role of energy of fusion. Tables 6.1 and 6.2 show the physical and numerical parameters utilized in this analysis.

Table 6.1: Variables and Parameters in Permafrost Modeling

Symbol	**Value**	**Description**	**Units**
z	–	Depth	m
t	–	Time	s
$E(z,t)$	–	Energy density	$\frac{MJ}{m^3}$
$q(z,t)$	–	Energy flux	$\frac{MW}{m^2}$
$T(z,t)$	–	Temperature	°C
E_{fus}	0.334	Energy of fusion	$\frac{MJ}{m^3}$
β_{sol}	22.2	Reciprocal of volumetric heat capacity (solid)	$\frac{Km^3}{MJ}$
β_{liq}	22.2	Reciprocal of volumetric heat capacity (liquid)	$\frac{Km^3}{MJ}$
κ_{sol}	1×10^{-6}	Thermal conductivity (solid)	$\frac{MW}{mK}$
κ_{liq}	1×10^{-6}	Thermal conductivity (liquid)	$\frac{MW}{mK}$
η	0.085×10^{-6}	Effective derivative times conductivity	$\frac{MW}{m^2}$
M	1000	Depth	m

The spatial and temporal discretization parameters were chosen to balance computational efficiency with accuracy:

Table 6.2: Spatial and Temporal Discretization Parameters

Parameter	**Value**	**Description**
Depth (M)	1000 m	Total column depth
Number of boxes (n_{boxes})	300	Spatial discretization units
Box height (Δz)	3.33 m	Height per box
Time step (dt)	$1/(12{\cdot}4{\cdot}7)$ yr	≈ 1.09 days
Simulation duration (t_{final})	200 yr	Total simulation time
Global warming rate	0.03 °C/yr	3 °C per 100 years

6.2 Thermal Evolution Results

Using parameters comparable to Hill's model (Table 3.2.2), we investigated the impact of the energy of fusion on permafrost thawing patterns. With minimal energy of fusion, 0.334 $\frac{MJ}{m^3}$, only one thousandth of water's fusion energy, our model shows a temperature evolution pattern similar to Hill's while also revealing unique characteristics (Figure 6.1). Both models exhibit bottom-up thawing progression, evidenced by the advancing warm front visible in the temperature contours. Our model predicts complete melting in about 58 years, consistent with Hill's temporal scale.

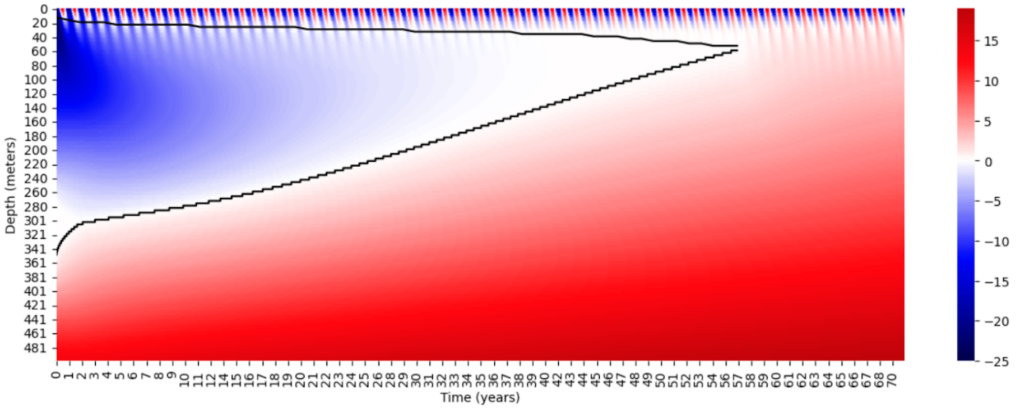

Figure 6.1: Energy Flow Model Base case

A preliminary analysis explored E_{fus} values from 0.49 to 2.90 $\frac{MJ}{m^3}$. Meltline trajectories (Figure 6.2) indicate deepening initial ice formation with higher energy of fusion, as evidenced by the lower meltline starting points shifting downward from about 100 meters at $E_{fus} = 0.49$ $\frac{MJ}{m^3}$ to 175 meters at $E_{fus} = 2.90$ $\frac{MJ}{m^3}$.

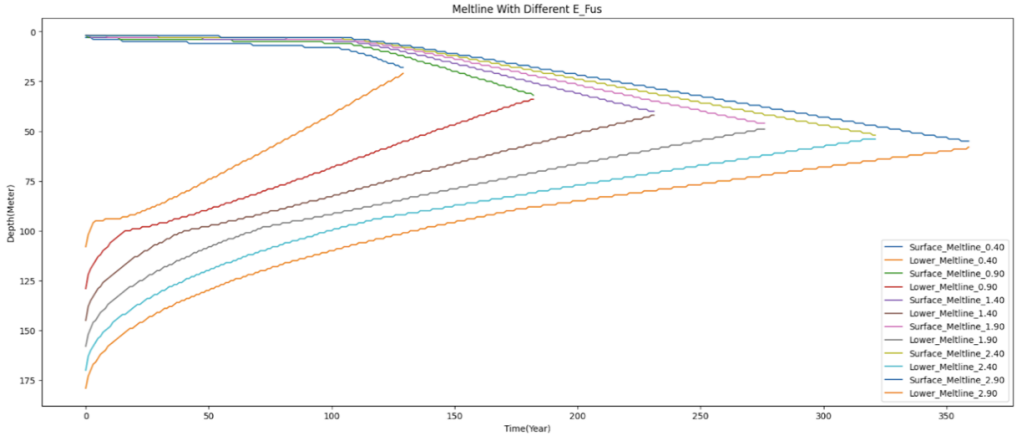

Figure 6.2: Permafrost Meltlines for Increasing Energy of fusion

Results reveal a non-linear relationship between energy of fusion and thawing

rates (Figure 6.3). The time to melt increases from 125 years at $E_{fus} = 0.49\ \frac{MJ}{m^3}$ to 175 years at $E_{fus} = 0.90\ \frac{MJ}{m^3}$, then to 225 years at $E_{fus} = 1.40\ \frac{MJ}{m^3}$ and 275 years at $E_{fus} = 1.90\ \frac{MJ}{m^3}$. The most dramatic comparison exists between extreme cases: permafrost with minimal water content (0.334 MJ/m^3) that melts in about 58 years, and water-equivalent permafrost (334 MJ/m^3) which takes 8,956 years to melt.

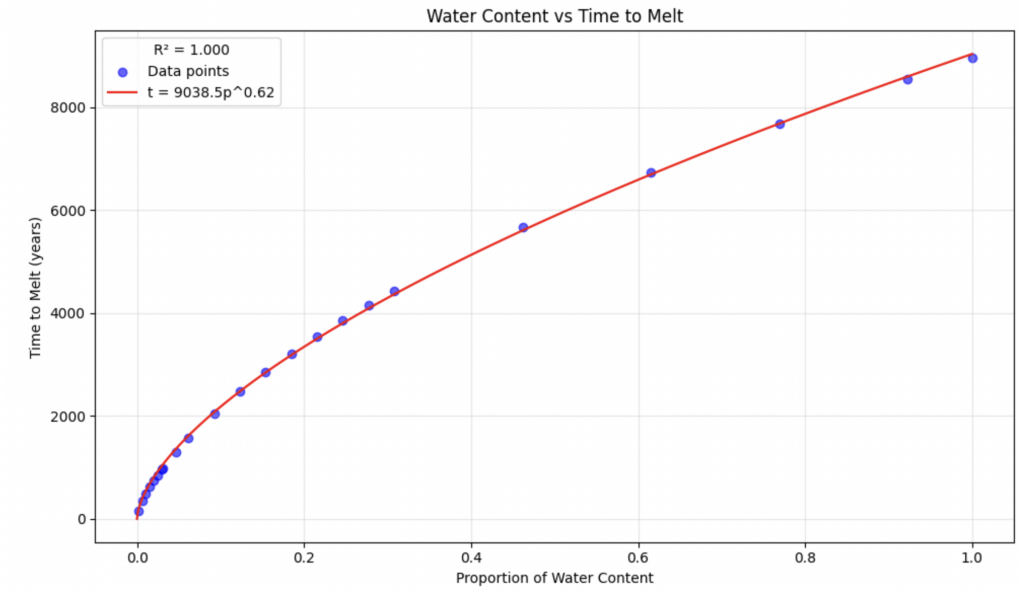

Figure 6.3: Energy of fusion vs. Time to melt

6.3 Justification for Updated Parameters Based on Field Measurements

Our initial simulations used parameters from Hill's temperature-based model for direct comparison. To better reflect actual permafrost conditions, we updated key

parameters based on field measurements by Sun et al. [9] This section justifies these revisions.

6.3.1 Heat Capacity Parameters

The original model used identical reciprocal heat capacity values for both frozen and thawed states ($\beta_{sol} = \beta_{liq} = 22.2\ \frac{Km^3}{MJ}$). Field measurements by Sun et al. showed varied volumetric heat capacities, with frozen soil between 1500-2100 $\frac{kJ}{m^3 \cdot C}$ and thawed soil between 1900-2900 $\frac{kJ}{m^3 \cdot C}$. Converting these to reciprocal heat capacities in our model's units yields:

$$\beta_{sol} = \frac{1}{2.119} \frac{km^3}{MJ} (\text{frozen})$$

$$\beta_{liq} = \frac{1}{2.927} \frac{km^3}{MJ} (\text{thawed})$$

This update captures two critical relationships: the higher inverse volumetric heat capacity of thawed soil ($\beta_{sol} > \beta_{liq}$) and a frozen/thawed ratio ($\beta_{sol}/\beta_{liq} \approx 1.38$) consistent with field observations.

6.3.2 Thermal Conductivity Parameters

Our model assumed identical thermal conductivities for frozen and thawed states ($\kappa_{sol} = \kappa_{liq} = 1 \times 10^{-6}\ \frac{W}{mK}$). Sun et al.'s measurements showed distinct ranges: frozen soil had conductivities of 1.25-2.80 $\frac{W}{m \cdot C}$, while thawed soil ranged from 0.85-2.10 $\frac{W}{m \cdot C}$. In model units, we updated to:

$$\kappa_{sol} = 2 \times 10^{-6} \frac{MW}{mK}$$

$$\kappa_{liq} = 1.5 \times 10^{-6} \frac{MW}{mK}$$

This revision accurately reflects higher thermal conductivity in frozen soil, sets a realistic frozen/thawed conductivity ratio ($\kappa_{sol}/\kappa_{liq} \approx 1.33$), and keeps values within the observed range for permafrost soils.

6.3.3 Geothermal Heat Flux Parameter

The effective thermal gradient parameter (η) was revised using Sun et al.'s geothermal measurements from two sites. The Xidatan site exhibited a gradient of 0.062 $\frac{^\circ C}{m}$, while the Tanggula site measured 0.040 $\frac{^\circ C}{m}$. Applying Fourier's law and the average thermal conductivity, we calculated:

$$\eta = 0.124 \times 10^{-6} \text{ MW/m}^2$$

This update from the original value (0.085×10^{-6} $\frac{MW}{m^2}$) directly connects to field measurements, ensures consistency with geothermal gradients, and better represents heat flux in permafrost.

6.3.4 Model Depth Selection

The original 1000-meter depth was reduced to 100 meters based on Sun et al.'s observations. They found a maximum permafrost base of 67 m at the Tanggula site, with temperature measurements to 34.5 m depth. Century-scale climate effects are generally limited to the upper 100 m of permafrost. This revision aligns with actual permafrost depths and also improves computational efficiency while preserving depth for thermal processes.

6.3.5 Upper Boundary Condition

The periodic temperature boundary condition was maintained, with parameters adjusted for field conditions. We used a mean temperature of -5°C, an annual amplitude of 20°C, and a warming rate of 0.03°C/year. These values align with Sun et al.'s observations while preserving the model's capability to capture seasonal variations and long-term warming trends.

6.3.6 Energy of Fusion Parameter

The energy of fusion parameter (E_{fus}) was redefined to represent water/ice content directly, using the energy of fusion of pure water/ice (334.54 MJ/m^3) as a reference. This change allows simulation of various permafrost conditions by adjusting the water content percentage.

6.4 Role of Water Content in Permafrost Thawing

The water/ice content of permafrost significantly influences its thermal behavior and thawing characteristics. We use the energy of fusion parameter (E_{fus}) as a proxy for water content to explore how varying ice concentrations influence permafrost degradation under warming conditions.

6.4.1 Energy of Fusion as Proxy for Water Content

Let L be the energy of fusion of pure water/ice, so we consider $L = 334.54\ \frac{MJ}{m^3}$. This value serves as a reference for relating energy of fusion to water content. In our model, the effective energy of fusion for a soil-ice mixture scales linearly with volumetric water content (w):

$$E_{fus} = wL \tag{6.4.1}$$

where w indicates the volume fraction of water/ice in the soil (ranging from 0 to 1). This relationship allows simulating permafrost with varying water contents by adjusting E_{fus}. For instance, 50% water content in permafrost is represented by $E_{fus} = 167.3$ MJ/m^3, while 10% water content corresponds to $E_{fus} = 33.5$ MJ/m^3.

6.4.2 Water Content Effects on Thermal Properties

Permafrost's water/ice content influences its energy of fusion, thermal conductivity, and heat capacity. In our simulations, we maintain constant thermal properties

(κ_{sol}, κ_{liq}, β_{sol}, β_{liq}) while varying E_{fus} to isolate latent heat's impact on thawing dynamics. This approach clarifies the role of phase change in thaw progression.

Using field measurements from Sun et al., we implemented thermal conductivities of $\kappa_{sol} = 2 \times 10^{-6}$ MW/mK for frozen soil and $\kappa_{liq} = 1.5 \times 10^{-6}$ MW/mK for thawed soil, with reciprocal heat capacities of $\beta_{sol} = 1/2.119$ and $\beta_{liq} = 1/2.927$ Km^3/MJ. These values represent standard permafrost soil properties and are consistent across water content variations.

6.4.3 Systematic Variation of Water Content

To investigate how water content affects permafrost thawing, we simulated 10%, 50%, and 90% water contents, corresponding to E_{fus} values of 33.5, 167.3, and 300.6 $\frac{MJ}{m^3}$. These cases span typical water contents in natural permafrost systems. Our base case used an effectively zero energy of fusion ($E_{fus} = 1 \times 10^{-12}$ MJ/m^3), representing dry soil.

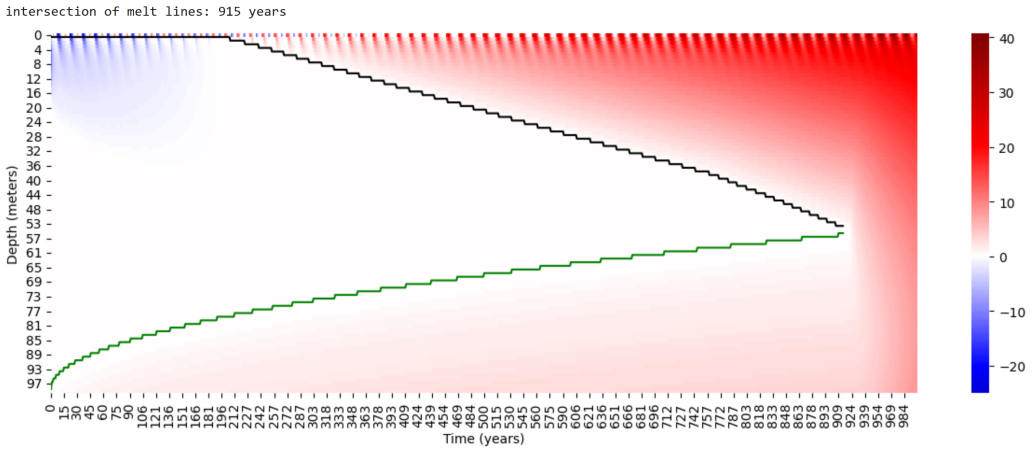

Figure 6.4: Temperature evolution for permafrost with 90% water content. The black line indicates the 0°C isotherm, showing the progression of the thawing front. The color scale represents temperature in °C, with blue indicating frozen conditions and red indicating thawed conditions.

Figure 6.4 shows the temperature evolution for permafrost with 90% water content. The simulation reveals a sharp thawing front that moves slowly through the soil column. High water content resists temperature change due to the substantial latent heat requirement, creating a clear boundary between frozen and thawed regions. The black line at 0°C illustrates the gradual downward progression of the thawing interface over several centuries.

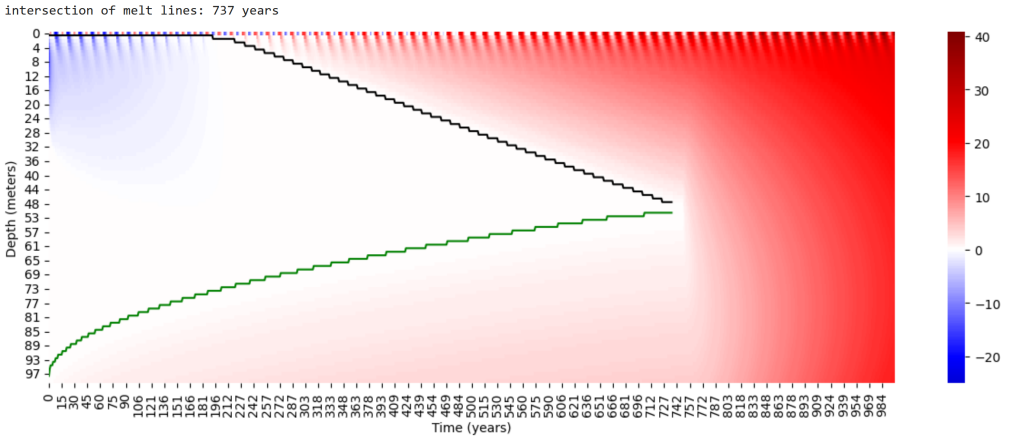

Figure 6.5: Temperature evolution for permafrost with 50% water content. The intermediate water content shows a balance between phase change and heat conduction effects. The color scale represents temperature in °C.

For 50% water content (Figure 6.5), the thawing pattern shows characteristics between high and low extremes. The thawing front is distinct and progresses faster than in the 90% case. Temperature contours reveal a wider transition zone between frozen and thawed states, indicating that heat conduction is more significant compared to phase change effects.

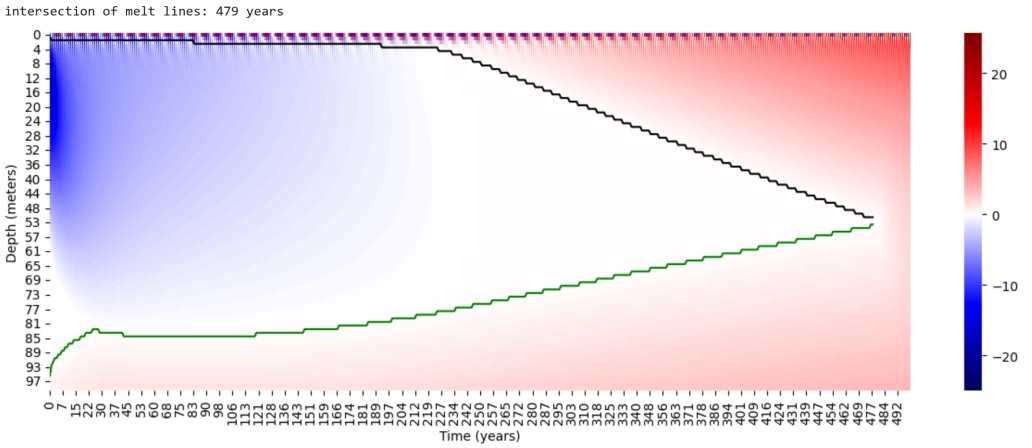

Figure 6.6: Temperature evolution for permafrost with 10% water content. The lower water content results in more diffuse thawing patterns dominated by heat conduction. The color scale represents temperature in °C.

The 10% water content case (Figure 6.6) exhibits distinct behavior. The thawing front is less defined, and the temperature field shows a gradual transition between frozen and thawed states. Lower energy of fusion requirements enable faster temperature changes, leading to a diffuse thawing pattern dominated by heat conduction instead of phase change effects.

6.4.4 Analysis of Thawing Timescales

The simulation results show significant variation in thawing timescales based on water content. The case with minimal water content thaws completely in about 58 years, as shown in Figure 6.1. Conversely, the 10% water content case (Figure 6.6) takes 475 years for complete thawing. This nearly order-of-magnitude increase in thawing time demonstrates the substantial impact of even modest ice content on permafrost stability.

Thawing time increases with water content, reaching 737 years for 50% and 911 years for 90% (Figures 6.5 and 6.4). This non-linear relationship underscores the energy of fusion's role in resisting permafrost degradation. Nonetheless, the relative increase in thawing time diminishes at higher water contents, indicating a saturation effect.

The temperature contours in Figures 6.4-6.6 reveal various thawing patterns. Higher water content cases show distinct phase change fronts slowly moving through the soil column, evident as compressed contour lines around the 0°C isotherm. In contrast, lower water content cases display diffuse thawing zones with gradually spaced contours, indicating that heat conduction prevails over phase change effects.

These results show that accurately representing ground ice content is vital for predicting permafrost response to climate warming. Order-of-magnitude differences in thawing timescales indicate that small variations in ice content significantly affect permafrost vulnerability to degradation. The presence of ice, rather than its exact quantity, is the key factor in determining permafrost resilience to warming.

Chapter 7

Conclusion and Future work

7.1 Summary

This thesis presents a comprehensive analysis of permafrost dynamics through progressively sophisticated modeling approaches. Beginning with the Budyko-Sellers framework on global temperature-permafrost relationships, we progressed to Hill's heat diffusion model and then to Sun et al.'s empirical approach with phase transitions. We propose a energy based framework that emphasizes phase changes in permafrost thaw. By focusing on energy, our model captures the physics of phase transitions while ensuring computational efficiency. We demonstrated that water content affects permafrost degradation, with time to melt ranging from decades to millennia based on ice content. Simulations indicate that permafrost with 10% water content thaws in about 475 years, while 90% water content takes 911 years, highlighting the role of latent heat in thermal resistance. These findings suggest

that current climate models may need to better account for spatial variations in permafrost water content to accurately predict carbon release timing.

The key innovation of our framework is its unified approach to permafrost physics through conservation laws. The model's energy flow formulation eliminates distinctions between frozen and thawed states, allowing continuous evolution of thermal properties based on the system's energy state. The discretization scheme ensures numerical stability and enables efficient century scale permafrost evolution simulation. Validated with Qinghai-Tibetan plateau field measurements, the model accurately reproduced the complex thermal behaviors of natural systems. It notably captured the *zero curtain* effect, where temperature remains near 0°C during phase transitions— a phenomenon often missed by temperature-based models. This improved physical representation provides a more reliable foundation for incorporating permafrost dynamics into global climate models, especially for regions where traditional models underestimate thaw rates and subsequent carbon release.

7.2 Permafrost Carbon Feedback: Regional Vulnerabilities and Global Climate Implications

According to recent NOAA data [10], northern permafrost soils store 1,460 to 1,600 gigatons of organic carbon, about double the atmospheric total. Approximately 1,035 gigatons, with a variation of 150 gigatons, is in the surface layer (0-3 m depth), constituting a significant portion of Earth's soil carbon. Permafrost regions

contribute 50% to the global soil carbon inventory while covering only 15% of total soil area.

Our analysis reveals a critical feedback mechanism: sporadic permafrost, especially in lower latitudes, is vulnerable to thaw. This concern escalates due to significant carbon accumulation in surface layers, as shown in Figure 7.1. The correlation between rapid thaw potential and high carbon concentration fosters an accelerated climate feedback loop, where thawing releases carbon, causing further warming and increased thaw rates.

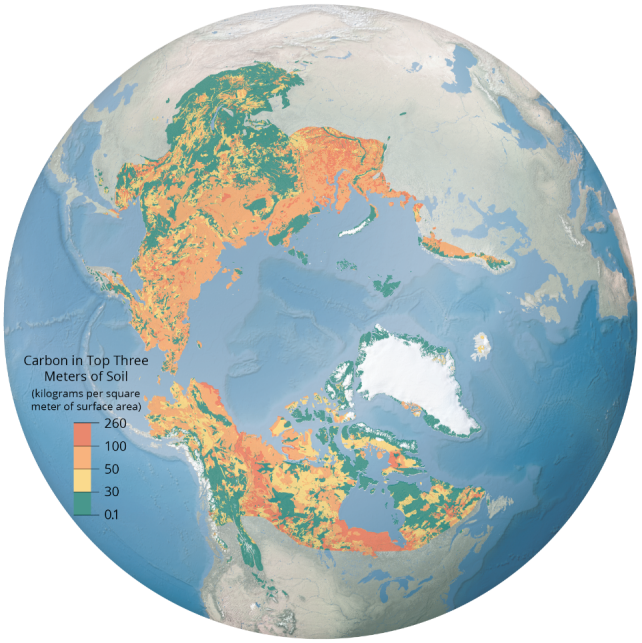

Figure 7.1: Soil organic carbon pools (0-3 m depth) for the northern circumpolar permafrost region. (modified from Scientific American, November 2016) from [10]

Regional vulnerability assessment identifies North America and parts of Asia as highly susceptible to rapid permafrost degradation. Lower water content in these

areas correlates with higher carbon concentrations, suggesting carbon release may occur faster than current climate models predict. This finding has major implications for climate modeling: projections may need significant revision to account for the relationship between water content and thawing rates, likely underestimating permafrost's contribution to the global carbon cycle.

The policy implications of these findings are significant. First, accelerated carbon release from permafrost indicates that emission reduction targets must be more ambitious. Second, monitoring and protection should prioritize areas with low water content and high carbon concentrations due to their elevated risk for rapid carbon release. Finally, the non-linear relationship between water content and thaw rates highlights the urgent need for effective climate mitigation strategies to avoid potential tipping points in permafrost stability.

These insights emphasize the need to include energy of fusion in permafrost models, particularly for carbon-rich regions with low ice content. With rising global temperatures, accurate modeling of permafrost thaw dynamics is crucial for climate projections and policy decisions to mitigate climate change impacts.

7.3 Limitations and Future Research Directions

While our energy-based framework offers insights into permafrost thaw dynamics, several limitations and future research opportunities require discussion. Our model, like Hill's conceptual approach, employs certain simplifying assumptions that could

be refined in future work. These include treating soil properties as homogeneous within phases, assuming purely vertical heat flow, and omitting hydrological processes that may impact thaw patterns.

The model's parameterization can improve with better integration of field data. Currently, thermal conductivity and heat capacity are treated as phase-dependent constants, but real permafrost systems show complex variations with temperature, pressure, and composition. Following Sun et al.'s approach [9], future work should incorporate depth-dependent thermal properties and more sophisticated representations of unfrozen water content effects.

A sensitivity analysis would greatly improve our understanding of the model's behavior and limitations. This analysis should examine the influence of key parameters, including thermal diffusivity (k), lower boundary temperature (M), and temperature forcing (F) within realistic ranges. Such an investigation will offer insights into how these parameters influence predictions of permafrost thaw patterns and gas release mechanisms, particularly regarding the formation of permafrost craters in the Yamal Peninsula [5].

Integration with global climate models represents another important direction for future research. Our model captures local-scale thaw dynamics, coupling it with other climate models would enhance predictions of regional and global carbon feedback mechanisms. This integration would require:

- Development of efficient upscaling methods to translate local thaw dynamics

to regional scales

- Implementation of two-way coupling between permafrost thaw and atmospheric processes
- Incorporation of vegetation and hydrological feedbacks

Additional data needed for model validation include:

- High-resolution temporal and spatial measurements of permafrost temperature profiles
- Detailed characterization of soil composition and water content variations with depth
- Long-term monitoring of thaw progression in diverse permafrost environments
- Quantification of gas release rates from thawing permafrost

Future work should address limitations in our current approach. Addressing these limitations and pursuing these research directions would enhance the model's predictive capabilities and understanding of permafrost-climate feedbacks. A key focus is developing advanced parameterization schemes that consider the heterogeneous nature of permafrost systems while ensuring computational efficiency.

7.4 Concluding Remarks

This work reveals the critical relationship between water content and thaw rates, challenging assumptions about permafrost degradation timing and carbon release. The climate modeling community must now consider that carbon feedback from permafrost regions may occur more rapidly than estimated, especially in discontinuous permafrost areas with lower water content. This understanding shifts our view of the Arctic's role in climate change, suggesting a narrower window for effective climate action than current models indicate.

Chapter 8

Acronyms and Glossary

Care has been taken in this thesis to minimize the use of jargon and acronyms, but this cannot always be achieved. This appendix defines jargon terms in a glossary and contains a table of acronyms and their meanings.

8.1 Glossary

Abundant Energetic Particles High-energy particles originating outside of the Earth's atmosphere, often associated with cosmic rays.

Active Layer The top layer of soil in permafrost regions that thaws and refreezes seasonally.

Albedo (α) The fraction of solar energy reflected by a surface, influencing heat absorption and climate dynamics.

Cryopeg Lenses of highly saline, unfrozen water found within permafrost.

Dirichlet Boundary Conditions A type of boundary condition in mathematical modeling where the value of a function is fixed on the boundary of the domain.

Energy of Fusion (Efus) The amount of energy required to change a unit mass of a substance from solid to liquid.

Geothermal Heat Flux Heat emanating from the Earth's interior, contributing to the thermal dynamics of the soil.

Heat Equation A partial differential equation that describes the distribution of heat (or temperature) in a given region over time.

Latent Heat Energy absorbed or released during a phase change (e.g., freezing or thawing) without a change in temperature.

Mantle The layer of the Earth between the crust and the core, composed primarily of silicate rocks and minerals.

Neumann Boundary Conditions A type of boundary condition where the derivative of a function is specified on the boundary of the domain, representing the rate of change.

Phase Transition The process of changing between solid, liquid, and gaseous states.

Representative Concentration Pathways (RCP) Climate scenarios describing potential greenhouse gas concentration trajectories and their impacts on global warming.

Thermal Conductivity (κ) A measure of a material's ability to conduct heat.

Volumetric Heat Capacity The amount of heat required to raise the temperature of a unit volume of a material by one degree.

Zero Curtain Effect A phenomenon in permafrost where the temperature remains near 0°C during phase changes due to latent heat absorption or release.

8.2 Acronyms

Table 8.1: Acronyms and their meanings

Acronym	Meaning
IPCC	Intergovernmental Panel on Climate Change
AR6	Intergovernmental Panel on Climate Change Sixth Assessment Report
NSIDC	National Snow and Ice Data Center
ESMs	Earth System Models
EBM	Energy Balance Model

Continued on next page

Table 8.1 – continued from previous page

Acronym	Meaning
RCP	Representative Concentration Pathways
CRU	Climatic Research Unit
CL	Climatic Layers
AGU	American Geophysical Union

References

[1] Christina Nunez. Permafrost: Everything you need to know. `https://www.nrdc.org/stories/permafrost-everything-you-need-know`, 2019. Accessed: 2025-02-20.

[2] Edward AG Schuur, James Bockheim, Josep G Canadell, Eugenie Euskirchen, Christopher B Field, Sergey V Goryachkin, Stefan Hagemann, Peter Kuhry, Peter M Lafleur, Hanna Lee, et al. Vulnerability of permafrost carbon to climate change: Implications for the global carbon cycle. *BioScience*, 58(8):701–714, 2008.

[3] National Snow and Ice Data Center. Why frozen ground matters. Accessed: 2025-02-20.

[4] John Nguyen and Aileen Zebrowski. Adapting the budyko model to analyze permafrost recession and potential for carbon feedback. *SIAM Undergraduate Research Online*, 14, 2020.

[5] Sergey N Buldovicz, Vanda Z Khilimonyuk, Andrey Y Bychkov, Evgeny N Ospennikov, Sergey A Vorobyev, Aleksey Y Gunar, Evgeny I Gorshkov, Evgeny M Chuvilin, Maria Y Cherbunina, Pavel I Kotov, et al. Cryovolcanism on the earth: Origin of a spectacular crater in the yamal peninsula (russia). *Scientific reports*, 8(1):1–6, 2018.

[6] Kaitlin Hill and Richard McGehee. Heat conduction through permafrost and its potential for explosive behavior. *arXiv preprint arXiv:1810.12370*, 2018.

[7] Boris K Biskaborn, Sharon L Smith, Jeannette Noetzli, Heidrun Matthes, Gonçalo Vieira, Dmitry A Streletskiy, Philippe Schoeneich, Vladimir E Romanovsky, Antoni G Lewkowicz, Andrey Abramov, et al. Permafrost is warming at a global scale. *Nature communications*, 10(1):1–11, 2019.

[8] American Geophysical Union. New mechanism revealed for mysterious craters in siberian permafrost. `https://news.agu.org/press-release/new-yamal-craters-explanation/`, 2024. AGU News Press Release.

[9] Zhe Sun, Lin Zhao, Guojie Hu, Yongping Qiao, Erji Du, Defu Zou, and Changwei Xie. Modeling permafrost changes on the qinghai–tibetan plateau from 1966 to 2100: A case study from two boreholes along the qinghai–tibet engineering corridor. *Permafrost and Periglacial Processes*, 31(1):156–171, 2020.

[10] T Schuur. Permafrost and the global carbon cycle. *Arctic Report Card 2019*, 58, 2019.

[11] A. Pirani et al Masson-Delmotte V., P. Zhai. Ipcc 2021: Climate change 2021: The physical science basis. contribution of working group i to the sixth assessment report of the intergovernmental panel on climate change. (6), 2021.

[12] Christina Schädel, Brendan M Rogers, David M Lawrence, Charles D Koven, Victor Brovkin, Eleanor J Burke, Hélène Genet, Deborah N Huntzinger, Elchin Jafarov, A David McGuire, et al. Earth system models must include permafrost carbon processes. *Nature Climate Change*, pages 1–3, 2024.

[13] Mikhail I Budyko. The effect of solar radiation variations on the climate of the earth. *tellus*, 21(5):611–619, 1969.

[14] William D Sellers. A global climatic model based on the energy balance of the earth-atmosphere system. *Journal of Applied Meteorology and Climatology*, 8(3):392–400, 1969.

[15] Anna M Barry, Esther Widiasih, and Richard McGehee. Nonsmooth frameworks for an extended budyko model. *arXiv preprint arXiv:1406.6028*, 2014.

[16] Ka-Kit Tung. *Topics in mathematical modeling*. Princeton University Press, 2016.

[17] Petr Chỳlek and JA Coakley Jr. Analytical analysis of a budyko-type climate model. *Journal of Atmospheric Sciences*, 32(4):675–679, 1975.

[18] Gerald R North. Analytical solution to a simple climate model with diffusive heat transport. *Journal of Atmospheric Sciences*, 32(7):1301–1307, 1975.

[19] Richard McGehee and Esther Widiasih. A quadratic approximation to budyko's ice-albedo feedback model with ice line dynamics. *SIAM Journal on Applied Dynamical Systems*, 13(1):518–536, 2014.

[20] Sonja Kaiser, Mathias Göckede, Karel Castro-Morales, Christian Knoblauch, Altug Ekici, Thomas Kleinen, Sebastian Zubrzycki, Torsten Sachs, Christian Wille, and Christian Beer. Process-based modelling of the methane balance in periglacial landscapes (jsbach-methane). *Geoscientific Model Development*, 10(1):333–358, 2017.

[21] Daniel Riseborough, Nikolay Shiklomanov, Bernd Etzelmüller, Stephan Gruber, and Sergei Marchenko. Recent advances in permafrost modelling. *Permafrost and Periglacial Processes*, 19(2):137–156, 2008.

[22] Marina O Leibman, Alexander I Kizyakov, Andrei V Plekhanov, and Irina D Streletskaya. New permafrost feature–dep crater in central yamal (west siberia, rusia) as a response to local climate fluctuations. *Geography, environment, sustainability*, 7(4):68–79, 2014.

[23] Pingkang Wang, Xuhui Zhang, Youhai Zhu, Bing Li, Xia Huang, Shouji Pang, Shuai Zhang, Cheng Lu, and Rui Xiao. Effect of permafrost properties on gas hydrate petroleum system in the qilian mountains, qinghai, northwest china. *Environmental Science: Processes & Impacts*, 16(12):2711–2720, 2014.

[24] Mark New, David Lister, Mike Hulme, and Ian Makin. A high-resolution data set of surface climate over global land areas. *Climate research*, 21(1):1–25, 2002.

[25] Trond Slagstad, Kirsti Midttømme, Randi Kalskin Ramstad, and Dag Slagstad. Factors influencing shallow (less than 1000 m depth) temperatures and their significance for extraction of ground-source heat. *Geology for society. Spec. Publ*, 11:99–109, 2008.

[26] Omar T Farouki. The thermal properties of soils in cold regions. *Cold Regions Science and Technology*, 5(1):67–75, 1981.

[27] Arthur H Lachenbruch and B Vaughn Marshall. Changing climate: geothermal evidence from permafrost in the alaskan arctic. *Science*, 234(4777):689–696, 1986.

[28] David M Lawrence, Andrew G Slater, Vladimir E Romanovsky, and Dmitry J Nicolsky. Sensitivity of a model projection of near-surface permafrost degradation to soil column depth and representation of soil organic matter. *Journal of Geophysical Research: Earth Surface*, 113(F2), 2008.

[29] Elchin E Jafarov, Sergey S Marchenko, and VE Romanovsky. Numerical modeling of permafrost dynamics in alaska using a high spatial resolution dataset. *The Cryosphere*, 6(3):613–624, 2012.

[30] Sebastian Westermann, Moritz Langer, Julia Boike, Max Heikenfeld, Maria Peter, Bernd Etzelmüller, and Gerhard Krinner. Simulating the thermal regime

and thaw processes of ice-rich permafrost ground with the land-surface model cryogrid 3. *Geoscientific Model Development*, 9(2):523–546, 2016.

[31] Ana MO Morgado, Luis AM Rocha, Julyan HE Cartwright, and Silvana SS Cardoso. Osmosis drives explosions and methane release in siberian permafrost. *Geophysical Research Letters*, 51(18):e2024GL108987, 2024.

[32] Samuel I. Outcalt, Frederick E. Nelson, and Kenneth M. Hinkel. The zero-curtain effect: Heat and mass transfer across an isothermal region in freezing soil. *Water Resources Research*, 26(7):1509–1516, 1990.

[33] Rubinšteĭ. *The stefan problem*.

[34] DJ Nicolsky and Vladimir E Romanovsky. Modeling long-term permafrost degradation. *Journal of Geophysical Research: Earth Surface*, 123(8):1756–1771, 2018.

[35] Naren Vohra and Malgorzata Peszynska. Modeling permafrost: Soil, ice, and some really hard mathematics. *SIAM News*, 2023.

[36] Scott L Painter, Ethan T Coon, Adam L Atchley, Markus Berndt, Rao Garimella, J David Moulton, Daniil Svyatskiy, and Cathy J Wilson. Integrated surface/subsurface permafrost thermal hydrology: Model formulation and proof-of-concept simulations. *Water Resources Research*, 52(8):6062–6077, 2016.

[37] Michelle A Walvoord and Barret L Kurylyk. Hydrologic impacts of thawing permafrost—a review. *Vadose Zone Journal*, 15(6):vzj2016–01, 2016.

[38] Virgil J Lunardini. *Heat transfer with freezing and thawing*. Elsevier, 1991.

[39] Yu L Shur and M Torre Jorgenson. Patterns of permafrost formation and degradation in relation to climate and ecosystems. *Permafrost and Periglacial Processes*, 18(1):7–19, 2007.

[40] Kevin Schaefer, Hugues Lantuit, Vladimir E Romanovsky, Edward AG Schuur, and Ronald Witt. The impact of the permafrost carbon feedback on global climate. *Environmental Research Letters*, 9(8):085003, 2014.

[41] T.E. Osterkamp and C.R. Burn. Permafrost. In James R. Holton, editor, *Encyclopedia of Atmospheric Sciences*, pages 1717–1729. Academic Press, Oxford, 2003.

Appendix A

Numerical Implementation Code

This appendix includes the Python implementation of the numerical solution for the Energy Flow Formulation used in this thesis.

A.1 Main Implementation

```
1 import numpy as np
2 import pandas as pd
3 from matplotlib import pyplot as plt
4 from matplotlib import colormaps
5 import seaborn as sns
6 import scipy.ndimage
7
```

```
# Parameters
E_fus = 300.6  # Water energy of fusion (MJ/m^3) #90% water content
beta_sol = 1/2.119  # reciprocal of the specific heat of the phase Km
    ^3/MJ
beta_liq = 1/2.927  # reciprocal of the specific heat of the phase Km
    ^3/MJ
kappa_sol = 2*10**(-6)  # thermal conductivity of solid MW/mK
kappa_liq = 1.5*10**(-6)  # thermal conductivity of liq MW/mK
eta = 0.124*10**(-6)  # effective derivative times thermal
    conductivity MW/m^2

M = 100  # depth meters
n_boxes = 99  # number of boxes
Delta_z = M / n_boxes  # height of each box

# global warming rate (degrees C per year)
drift_rate = 3/100  # for examples, 3 degrees per 100 years

# total length of simulation (years)
final_time = 1000

# size of time step (years)
dt = 1/12/4/7
```

Listing A.1: Packages and Parameters

A.2 Upper Boundary Condition

```
def upper_temp_boundary(t:float, drift_rate:float = 3/100):
    '''
    The upper periodic temperature boundary condition with linear
    upper trend drift.
    Sinusoidal fit at latitude 61.
    Param:
    t:float: time in years
    drift:float: the rate of global warming (degrees Celsius per year)
    '''
    periodic_term = -5 - 20 * np.cos(2*np.pi * t)
    drift_term = drift_rate * t
    return periodic_term + drift_term
```

Listing A.2: Upper boundary condition implementation

A.3 Energy Flow Equations

```
def theta_function(E):
    '''
    The three-step theta functions
    '''
    return np.where(E < 0, beta_sol*E,
           np.where((0 <= E) & (E <= E_fus), 0,
           beta_liq*(E-E_fus)))

```

```
9  def kappa_function(E):
10     '''
11     The three-step Kappa function
12     '''
13     return np.where(E < 0, kappa_sol,
14            np.where((0 <= E) & (E <= E_fus),
15            (kappa_sol*(E_fus-E) + kappa_liq*E)/E_fus,
16            kappa_liq))
17
18 def kappa_augmented(kappa_output):
19     '''
20     kappa constant for the j-th box calculated from the kappa function
       of energy
21     '''
22     kappas = np.zeros(n_boxes)
23     kappas[0] = kappa_output[0]
24     kappas[1:] = (kappa_output[0:-1] + kappa_output[1:])/2
25     return kappas
26
27 def q_augmented(T,kappas):
28     '''
29     the q constant output calculated from the temp and the
      kappa_augmented constant
30     '''
31     qs = np.zeros(n_boxes+1)
32     qs[0] = kappas[0]*(T[1]-T[0])/(Delta_z/2)
```

```
33      qs[1:-1] = kappas[1:]*(T[2:] - T[1:-1])/Delta_z
34      qs[-1]= eta  # lower boundary condition for q
35      return qs
36
37  def Vector_Field_f(q_values):
38      return (q_values[1:]-q_values[0:-1])/(Delta_z)
```

Listing A.3: Energy Flow Equations

A.4 Numerical Scheme

```
1   def Next_E_Values(E_Previous, T_Previous, dt):
2       '''
3       Calculate the next energy value from the current energy value.
4       '''
5       Kappa_Output = kappa_function(E_Previous)
6       Kappa_Average_Output = kappa_augmented(Kappa_Output)
7       q_List_Output = q_augmented(T_Previous, Kappa_Average_Output)
8       Vector_Field_Output = Vector_Field_f(q_List_Output)
9
10      # convert to rate of change per year
11      n_seconds_in_a_year = 365 * 24 * 60 * 60
12      Vector_Field_Output_in_years = n_seconds_in_a_year *
        Vector_Field_Output
13
14      # compute new energy
```

```
15      New_E = E_Previous + dt * Vector_Field_Output_in_years
16
17      return New_E
18
19  def sol(E_IC, final_time, dt = 1/12/30, drift_rate = 3/100):
20      """
21      E_IC: A length n_boxes array containing the initial condition for
        E
22      final_time: The total length of the simulation (years)
23      dt: The time step of the simulation (years)
24      drift_rate = the rate of global warming (degrees Celsius per year)
25      """
26      Niters = 1+int(final_time/dt)  # total number of iterations to
        simulate
27
28      matrixE = np.zeros((n_boxes, Niters))
29      matrixT = np.zeros((n_boxes + 1, Niters))
30
31      t = 0
32
33      for i in range(Niters):
34          if t == 0:
35              matrixE[:,0] = E_IC  # from initial condition
36              temp_boundary_value = upper_temp_boundary(t, drift_rate)
37              matrixT[0,0] = temp_boundary_value
38              matrixT[1:,0] = theta_function(E_IC)
```

```
        else:
            E_prev = matrixE[:,i-1]
            T_prev = matrixT[:,i-1]
            matrixE[:,i] = Next_E_Values(E_prev, T_prev, dt)
            temp_boundary_value = upper_temp_boundary(t, drift_rate)
            matrixT[0,i] = temp_boundary_value
            matrixT[1:,i] = theta_function(matrixE[:,i])

        t += dt

    return matrixE, matrixT
```

Listing A.4: Numerical algorithm

A.5 Plot of Heat Map with Permafrost Boundary

```
def get_meltlines(df):
    """
    Custom function to get the two melt lines, upper and lower
    df: matrix of temperatures
    """
    is_frozen = df <= 0

    def get_surface_meltline(df):
        is_surface_melting_point = is_frozen & ~is_frozen.shift(1,
    fill_value=True)
```

```
10      pos_surface_melt = is_surface_melting_point.apply(lambda x: x.
    values.argmax())
11      deepest_surface_melt_per_year = pos_surface_melt.groupby(
12          pos_surface_melt.index.astype(int)).max()
13      return deepest_surface_melt_per_year
14
15  def get_lower_meltline(df):
16      is_lower_melting_point = is_frozen & ~is_frozen.shift(-1,
    fill_value=True)
17      pos_lower_melt = is_lower_melting_point.apply(
18          lambda x: len(x.values) - x.values[::-1].argmax())
19      shallowest_lower_melt = pos_lower_melt.groupby(
20          pos_lower_melt.index.astype(int)).max()
21      return shallowest_lower_melt
22
23  surface_meltline = get_surface_meltline(df)
24  lower_meltline = get_lower_meltline(df)
25
26  intersection = ((lower_meltline - surface_meltline)).idxmin()
27  print('intersection of melt lines: ' + str(intersection) + ' years
    ')
28
29  if intersection > 0:
30      surface_meltline = surface_meltline.loc[:intersection-1]
31      lower_meltline = lower_meltline.loc[:intersection-1]
32
```

```
33      surface_meltline.index = surface_meltline.index/dt
34      lower_meltline.index = lower_meltline.index/dt
35
36      return surface_meltline, lower_meltline
```

Listing A.5: Plot of Heat Map with Permafrost Boundary